Materials Characterization 185 (2022) 111741

Contents lists available at ScienceDirect

Materials Characterization

journal homepage: www.elsevier.com/locate/matchar

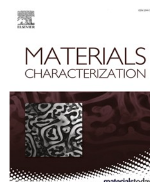

Application of advanced (S)TEM methods for the study of nanostructured porous functional surfaces: A few working examples

A.J. Santos [a,b,*], B. Lacroix [a,b], F. Maudet [c,1], F. Paumier [c], S. Hurand [c], C. Dupeyrat [d], V. J. Gómez [e,2], D.L. Huffaker [e,f], T. Girardeau [c], R. García [a,b], F.M. Morales [a,b,*]

[a] Department of Materials Science and Metallurgic Engineering, and Inorganic Chemistry, Faculty of Sciences, University of Cádiz, Spain
[b] IMEYMAT: Institute of Research on Electron Microscopy and Materials of the University of Cádiz, Spain
[c] Institut Pprime, UPR 3346 CNRS-Université de Poitiers-ENSMA, SP2MI, 86962 Futuroscope-Chasseneuil Cedex, France
[d] Safran Electronics and Defense, 26 avenue des Hauts de la Chaume, 86280 Saint-Benoît, France
[e] School of Engineering, Cardiff University, CF24 3AA Cardiff, United Kingdom
[f] School of Physics and Astronomy, Cardiff University, CF24 3AA Cardiff, United Kingdom.

ARTICLE INFO

Keywords:
Porous thin film
TEM sample preparation
HRTEM
iDPC-STEM
STEM spectroscopy
STEM-HAADF tomography

ABSTRACT

Nanostructured films offer the ability of modifying surface properties, even more, when they can generate layers with controlled porosity. The lower implicit integrity of these (multi)layers when compared to their compact counterparts, hinders the attainment of electron-transparent sections of submicron thicknesses (lamellae), which becomes one of the main reason for the scarcity of studies thorough (scanning-)transmission electron microscopy ((S)TEM). Aware of this opportunity, this report provides an overview of the possibilities offered by the application of a variety of (S)TEM techniques for the study of nanostructured and porous photonic surfaces. A few working examples are presented to illustrate the type of information that can be obtained in the case of mesoporous films prepared either by at oblique angles physical processes as well as nitride nanowire arrays prepared by epitaxy methods. It will be demonstrated that this approach enables the realization of several pioneering works, which are essential to complete the characterization of such porosity-controlled coatings. Topics as diverse as the preparation of electron-transparent specimens and the advanced characterization of their structures, morphologies, interfaces and compositions are addressed thanks to the implementation of new breakthroughs in (S)TEM, which allow to obtain high-resolution imaging, spectroscopies, or tomography, at both microscopic and nanoscopic levels. Finally, establishing (S)TEM as a reference tool for the advanced structural, chemical and morphological characterization of porous nanostructured skins, will open new horizons, providing better and new insights and thus allowing the optimization of the fabrication and design of such architectures.

1. Introduction

Surface engineering is an area of Materials Science & Technology that has lately attracted great interest thanks to the possibility of modifying the properties of the material that is covered by providing some characteristics that make it ideal for a determined application [1,2]. In this light, many different approaches have emerged, being the design and manufacturing of porosity-controlled coatings one of the most appealing, since they endow materials with improved and additional functionalities of interest in many fields such as energy [3,4], catalysis [5,6], optics [7–12] and electronics [13,14].

In recent times, coatings elaborated by means of oblique angle deposition (OAD) have become a widespread practice for attaining 3D micro- and mesoporous architectures of controlled structure and properties. Through this bottom-up approach, the deposition of porous films made of tilted nanocolumns (NCs) is achieved thanks to the shadowing effect that occurs when the incident flux of particles arrives at an oblique angle [15–20]. In this regard, OAD methods allow not only to deposit many types of materials (single elements, compounds with changing stoichiometries, metals, oxides, semiconductors, dielectrics, etc.) but

* Corresponding authors at: Department of Materials Science and Metallurgic Engineering, and Inorganic Chemistry, Faculty of Sciences, University of Cádiz, Spain.
E-mail addresses: antonio.santos@uca.es (A.J. Santos), fmiguel.morales@uca.es (F.M. Morales).

[1] Institute Functional Thin Film Oxides for Energy-efficient Future Information Technology, Helmholtz-Zentrum Berlin für Materialien und Energie Hahn-Meitner-Platz 1, 14,109 Berlin, Germany.

[2] Valencia Nanophotonics Technology Center, Universitat Politècnica de València, 46,022 València, Spain.

https://doi.org/10.1016/j.matchar.2022.111741
Received 15 July 2021; Received in revised form 5 December 2021; Accepted 10 January 2022
Available online 14 January 2022
1044-5803/© 2022 The Authors. Published by Elsevier Inc. This is an open access article under the CC BY-NC-ND license (http://creativecommons.org/licenses/by-nc-nd/4.0/).

also to sculpt, with a nanoscopic precision, a variety of complex architectures with controlled geometries (slanted, zig-zag, or helical structures; periodic arrays; etc.) simply by adjusting the deposition parameters during the deposition. Likewise, the manufacture of fine-controlled nanoporous films by molecular beam epitaxy (MBE) or chemical vapour deposition (CVD) methods has also shown to be a good approach, even though the architectures achieved by these two techniques are different from those generated by OAD methods, being the most significant those formed by nanorods (NRs) or nanowires (NWs) of semiconducting materials [21–24]. Within the framework of the development of nanostructures for ultra-high performance multifunctional devices, OAD and MBE techniques have proved to be powerful tools since both permit to tune the effective refractive index (*n*) of the deposited film by controlling the porosity of the system, enabling to manufacture broadband omnidirectional graded-refractive-index anti-reflective (AR) coatings [7–9,13,14,21,25–28]. Nevertheless, in order to take maximum benefits from these two approaches, a fine description at different scales of the elaborated systems is needed.

From the outset of these technologies, various techniques have been used to characterize such nanostructured films at different scales. In the case of the OAD structures, scanning electron microscopy (SEM) [29–31], atomic force microscopy (AFM) [32,33], X-ray diffraction (XRD) [34,35], or X-ray photoelectron spectroscopy (XPS) [36,37] studies have been extensively applied to obtain information about the structure, morphology and composition of such systems, which are relevant data to take into account for having a better description of their growth mechanisms and properties. It is however worth to point out that these techniques mentioned above provide microstructural information with a limited spatial resolution: several microns in the case of XRD and XPS and up to a few nanometers in the case of AFM (lateral resolution) and SEM. According to Hawkeye et al. [15], "the future development of OAD technology requires further study of fundamental growth processes as well as continued investigation and optimization of the physical properties of OAD fabricated films". Therefore, in order to advance on the knowledge of the fundamental processes involved in the generation of such type of nanostructured films and to go further into their performances optimization, it is now becoming essential to apply, in a systematic way, characterization methodologies that allow a fine description of these systems. In this context, transmission electron microscopy (TEM), and its related techniques, postulates as the appropriate candidate, which is known to be a powerful and fast-growing analytical tool to probe not only the local structure but also the local chemistry and morphology of materials.

In the past few years, the integration of efficient and multiple signal detectors combined with the arrival of aberration correctors for the electron lenses have enabled significant improvements related to elemental detection sensitivity and dramatic reduction of the attainable resolution limits below the Angstrom, opening up new possibilities and challenges in the characterization of materials [38–40]. However, although it has become a mainstay in the repertoire of characterization techniques for materials scientists, it should be noted that TEM still has difficulties to establish itself as a reference tool for apprehending topics related to nanoporous structures. Most of these difficulties come from the collection of electron-transparent sections of open (multi)layers of submicron thicknesses (lamellae), which becomes especially challenging compared to their compact equivalents. Besides, a thorough review of the state of the art dealing with the OAD processes indicates that only a few studies have concerned the application of TEM, most are restricted to very basic TEM analyses, including, mainly, conventional TEM imaging, electron diffraction, or high-resolution TEM (see the recent references [41–48] as example), and do not take advantage of the full potential of the ultimate generation electron microscopes including high spatial resolution imaging and spectroscopies or tomography for example.

On the other side, semiconducting nanowire films grown by MBE methods have also been broadly studied through SEM, photoluminescence spectroscopy (PL) or even TEM [49–57]. Nevertheless, as with the OAD systems, these works are limited to high-resolution and electron diffraction TEM studies of very narrow areas, being often observed the side faces and interfaces of individual NWs but not being explored the entire film or different representative areas, which can be associated to the aforementioned difficulties that the achievement of electron-transparent sheets of regular widths for nanoporous structures implies.

In this work, comprehensive studies by transmission and scanning-transmission electron microscopies ((S)TEM) were conducted on nanostructured porosity-controlled coatings, enabling several major advances, which were fundamental to reach important conclusions on the research of: (i) OAD systems of different nature, materials and architectures, providing not only a better insight of their structures and properties but also allowing the optimization of the fabrication and design of such architectures; and (ii) MBE films with variable morphologies and tunable optical and electrical properties of arrays of GaN hollow and/or compact nanowires. Issues as the preparation of electron-transparent specimens and the advanced characterization of their structures, morphologies, interfaces and compositions are discussed thanks to the implementation of new innovations in (S)TEM, which allow to obtain high resolution imaging, spectroscopies, or tomography, at both microscopic and nanoscopic levels.

2. Materials and methods

2.1. Sample fabrication

2.1.1. OAD films

A variety of OAD coatings prepared using different conditions and materials have been studied. Silicon dioxide (SiO_2) and titanium dioxide (TiO_2) OAD thin films were fabricated at room temperature in an electron-beam evaporator placed into a physical vapour deposition (PVD) vacuum chamber (base pressure 2×10^{-6} mbar). Such (multi) layers were deposited at different angles of incidence (α) relative to the substrate normal from 50° to 85°, without substrate rotation, by adjusting the angle of the substrate holder with respect to a fixed evaporation direction. Since this deposition chamber is not equipped with an in-situ adjustable orientation sample-holder, bilayer and trilayer systems were made in two and three steps respectively with an azimuthal rotation of $\Phi = 180°$ in between on silicon substrates. For a more in-depth description of deposition parameters of some of these systems, see references [8,9].

Indium tin-doped oxide (ITO) OAD films were fabricated at different angles α from 50 to 85° on silicon substrates by ion beam sputtering (IBS) deposition in a Nordiko chamber at room temperature with a base pressure of 2×10^{-6} Pa. The IBS chamber includes two radio-frequency sources: the first one was used to produce Ar or Xe ions accelerated at 1.2 keV, while the second one was employed as oxygen assistance gun with a flow of 5 sccm and the background pressure was maintained to 2 $\times 10^{-2}$ Pa. Further information on the IBS-OAD deposition of ITO films can be found elsewhere in reference [13].

2.1.2. Nanowire films by MBE

High-quality single crystalline GaN self-assembled NW films were grown on chemically cleaned p-type Si(111) or (100) substrates in a Veeco Gen930 molecular beam epitaxy (MBE) reactor along the [0001] direction and epitaxially aligned with the underlying Si substrate, following the same procedure as the one described in reference [21].

2.2. (S)TEM studies

To observe these materials under an electron beam, cross-sections (XTEM) of the specimens were prepared by two different methods: (i) a progressive thinning down by a tripod polisher (Model 590 Tripod Polisher®) up to few microns, followed by Ar^+ ion-milling at an

acceleration energy of 3.5 keV in a Gatan Precision Ion Polishing System (PIPS)-691 at ±7° milling angles (double-beam mode); (ii) the collection of electron-transparent lamellae using two different focused ion beam (FIB) systems: a Thermo Scientific Scios 2 DualBeam, and a ZEISS CrossBeam 350. Afterwards, such structures were studied by means of some advanced characterization techniques including high-angle annular dark field imaging (HAADF), electron tomography (ET), integrated differential phase contrast (iDPC) and local compositional analyses by EDX (energy-dispersive X-ray spectroscopy) and EELS (electron energy-loss spectroscopy). On this purpose, five different (S)TEM microscopes were used: JEOL 2100 LaB_6, JEOL 2010, FEI Talos F200S, FEI Talos F200X G2 and a double aberration-corrected FEI Titan Cubed Themis 60–300 microscope, working all of them at an accelerating voltage of 200 kV.

3. Results and discussion

Many nanoporous OAD and MBE systems of different nature, architecture and hardness will be here explored through the application of a wide variety of (S)TEM methods, giving special emphasis to (i) the most adequate procedures for the collection of electron-transparent sheets, (ii) overall studies of the structures and morphologies generated at micro- and nanoscale, (iii) atomic-resolution imaging of crystalline structures, (iv) chemical analyses by combining imaging and spectroscopies techniques, and (v) the 3D reconstruction of such structures by (S)TEM tomography.

3.1. Preparation of electron-transparent lamellae for (S)TEM observations

As previously mentioned, the fact that very few TEM based studies found for nanostructured thin films is closely linked to the difficulties encountered during the TEM sample preparation process. Besides, it becomes evident that the TEM sample preparation process of porous multilayer structures of dissimilar stiffness, such as the OAD ones, will be even more hindered. In order to lead the way for further TEM studies of porous nanostructured coatings, the challenging collection of electron-transparent lamellae of porous (multi)layers of different materials, architectures and hardness with methods of thinning down by tripod polishing plus ion milling, or focused ion beams (FIB) is here addressed. Moreover, the benefits and drawbacks of each sample preparation method are explored, paying special attention to aspects such as the homogeneity of the thinned lamella, the contamination during preparations, or the final thickness achieved.

3.1.1. Tripod polishing

As it is well-known, the TEM sample preparation process is a destructive method whose purpose is to collect an ultrathin specimen of a few nanometer-thick so that a beam of electrons is transmitted through it interacting with the specimen and forming the image. Traditionally, cross-section (XTEM) and planar-view (PVTEM) TEM sample preparation processes have been faced in many ways, although the majority of them share the following steps of cutting, grinding/polishing, dimpling and ion-milling [58–62]. Considering the relative weakness of the porous samples to be here studied, it is desirable to avoid the mechanical dimpling process since it would be quite severe [63]. Keeping this in mind, flat-type polishing of cross-sectional specimens were prepared using a tripod polisher, which allows to carefully thin down the specimen up to a few microns with a high control of micrometric steps applied on feet, evolving a much softer mechanical thinning than that achieved with heavy holders (as the Gatan Disc Grinder) and SiC sandpapers (as those of Struers), avoiding the dimpling stage and reducing the time required for the final thinning step by ion milling [64].

As can be seen in Fig. 1(a), specimen slats were cut into volume sizes of 2.5 mm × 0.8 mm. After that, two of these slats were glued (facing the

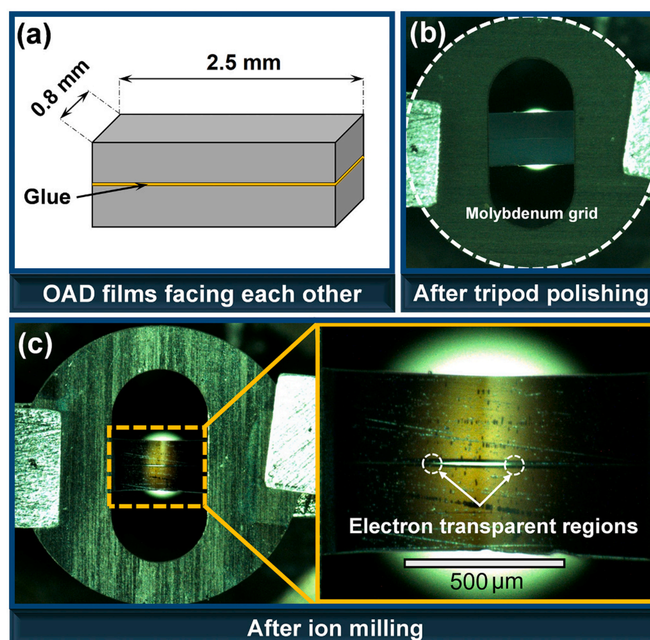

Fig. 1. Different stages involved in preparing delicate TEM specimens using the tripod method. (a) Scheme of a glued staked specimen before polishing. Pictures of the specimen, once attached to a 3 mm TEM molybdenum grid, after tripod polishing (b) and after ion milling (c). The inset of (c) places emphasis on the developed electron-transparent region.

porous films each other) using M-Bond 610 adhesive (Micro-Measurements). Once the epoxy adhesive is cured, the stacked specimen is fixed on the outer edge of the Pyrex glass stub, which is mounted on the tripod polisher by means of an L-bracket, using thermal wax, placing the plane formed by the two porous films perpendicular to the Pyrex glass surface. Once the thermal wax is cooled down, the excess is removed by applying acetone carefully. The latter is very important since the aspect and thickness of the specimen after each polishing step will be checked through an optical microscope which has the spindle of a micrometer attached that controls the thickness of the sample by means of the difference of focus between the polished surface of the sample and the Pyrex glass surface (free of thermal wax).

Before starting the polishing, it is necessary to level the tripod polisher which is done by manipulating the micrometers installed in its structure allowing to adjust the height of its supporting feet. Next, the both sides of the specimen are polished using successively 15, 6, 3, 1, and 0.5 μm grain diamond lapping films (South Bay Technology) by removing the material equivalent to three times the grain size from the previous stage (the “rule of three”) [65]. Here is very important to keep both specimen and diamond discs clean during polishing since otherwise bits of the sample that is being polished off or the remains of bigger diamond grains will cause scratches. In order to prevent that, the sample is cleaned between each polishing step by compressed air, while the remains of specimen retained on the diamond lapping films are removed after each step by using fresh paper towels. The specimen is polished until its thickness reaches 10–15 μm, then gluing a TEM grid on its top surface by applying small droplets of the M-Bond adhesive and letting it cure. Finally, the thinned specimen is easily removed from the Pyrex glass together with the glued grid by the immersion of the L-bracket in acetone. The aspect of a sample after polishing is shown in Fig. 1(b).

The supported sample is later undergone to a low-energy ion milling (3–3.5 kV) using a Gatan 691 PIPS system working at double beam mode (±7° milling angles). It must be taken into account that the milling parameters depend on the specimen material. Therefore, the milling conditions here provided can vary slightly depending on the characteristics of specimen to be prepared. Fig. 1(c) displays the final aspect of

a sample after half an hour of ion milling. As can be seen here, it was not carried out an excessive ion milling stage and that is the reason why the electron transparent region presents an elongated shape and not the so characteristic hole. Indeed, a minimal and smooth ion milling is always recommended not only to reduce sample damage but also to prevent the amorphization of the electron transparent area. This is helped by using a tripod polisher since, unlike the traditional polishing plus dimpling, it enables to thin down the specimen stack homogeneously up to 5–10 μm, reducing the time required for the ion milling step and favouring the generation of homogeneous electron transparent regions. The above emphasises with the homogeneously distributed yellow hue of both silicon substrate sheets that can be seen in the inset of Fig. 1(c), which reveal that the final thickness of the sample is suitable and that the ionic attack has occurred homogeneously and well-aligned.

3.1.2. FIB methods

FIB–TEM specimen preparation technique is another simple and straightforward alternative to collect electron-transparent lamellae of thin films. This technique not only provides the capability to prepare TEM samples with minimum levels of damage and contamination but is also capable of preparing samples either along particular orientations or in specific areas with a few nanometer precision [66]. From the beginning of this technique, the preparation of FIB-TEM samples of fragile or ultra-fine specimens has become a challenging issue. Nevertheless, the new cutting-edge techniques developed in recent years have helped to face these difficulties [67–69]. Following, the validity to prepare electron transparent lamellae of porous systems by means of FIB methods is here scrutinised.

Fig. 2 displays a TEM lamella fabricated by means of a FIB system. As can be seen in the picture, the lamella was thinned after lift-out with the aim of attaining ultra-thin regions, which is vital for collecting adequate high-resolution TEM images. The inset of Fig. 2 reveals a very good electron-transparent region for HRTEM observations after polishing at low energy but it implies an extra cost to pay: as can be noticed in the silicon substrate, a directional curtaining occurs as a result of the aforementioned polishing, giving rise to an irregular electron transparent region which could limit the conducting of some studies (i.e. to carry out 3D reconstructions by means of electron tomography methods). This does not mean that the FIB lift-out plus final thinning is not the most suitable approach to fabricate electron-transparent foils of porous thin films, but quite the opposite, since it sometimes becomes in the only one alternative to prepare them. In general, both tripod polishing and focused ion beams are good approaches to prepare electron-transparent sheets of porous coatings. Nevertheless, what is certain and evident is that, depending on the characteristics of the specimen to be studied and the TEM techniques to be applied, one approach can result more appropriate than the other one.

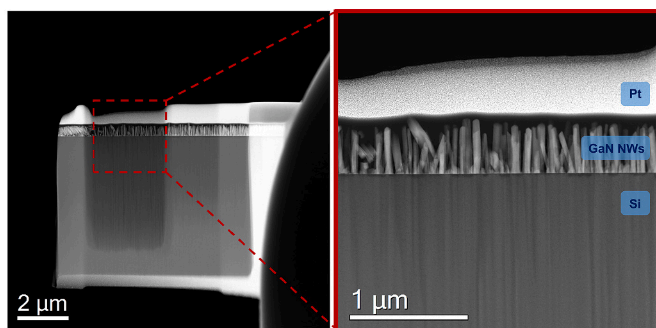

Fig. 2. STEM-HAADF overview of a FIB lamella of GaN nanowires. Note that the central part of the lamella was thinned and polished at low energy afterwards. The inset details the final aspect of the thinned region.

3.1.3. Selection of the most appropriate sample preparation process: advantages and drawbacks of both methods

Once evidenced that tripod polishing and FIB methods are both good approaches to collect electron-transparent regions of porous and delicate thin films, the next step will be to analyse which of these two alternatives would be the most appropriate one depending on the (S)TEM study to be conducted.

For this purpose, the advantages and disadvantages of one and other method are reviewed in Table 1. Initially, both methods will be compared from the point of view of the time invested to carry out a TEM preparation. As seen in previous sections, the tripod polishing method is a procedure that includes several stages, which have to be addressed systematically and thoroughly to achieve a satisfactory final result. Therefore, the preparation of a sample through this method usually takes, at best, 1–2 days for a trained person, but materials costs are low. In contrast, FIB sample preparation is more straightforward, faster (a specialized technician could carry out a FIB preparation in a few hours) and cleaner than the tripod polishing, since this method allows a lamella to be lifted out and thinned in the absence of glue, water, or other solvents. For that matter, it must be highlighted that such solvents have been proved to contribute to the oxidation of porous thin films of metalloids such as silicon and germanium but without affecting their structure and morphology [12]. Nevertheless, the time saved in FIB preparations is countered by the fact that the price of a preparation as well as the level of expertise required to carry out such experiment are both remarkably higher.

Now it is time to focus on the final appearance and electron transparency of cross-section specimens prepared by both methods, which were evaluated from relative thickness maps obtained by low-loss STEM EELS measurements and presented in Fig. 3 (for more information about this technique, refer to Section 3.4). The first electron transparent lamella (Fig. 3(a)) consists of a SiO_2 OAD bilayer prepared by means of tripod polishing plus ion-milling, while the second lamella (Fig. 3(b)) consists of a GaN NWs layer grown by MBE. As can be appreciated in Fig. 3(a), the observable region prepared by the mechanical approach is very thin, remains incredibly constant, and is maintained longitudinally over more than 4 μm ($t/\lambda \approx 0.3$ was measured across the NCs over the whole film, which corresponds to a specimen thickness of about 36 nm assuming an electron mean free path in SiO_2 of 120 nm according to our experimental conditions and to the Malis equation [70]). According to Fig. 3(b), FIB preparation of nanostructured porous films allows obtaining electron-transparent lamellae with extended ultra-thin areas comparable to tripod preparation as well ($t/\lambda \approx 0.3$ across the NWs, which corresponds to an absolute thickness of 27 nm assuming an

Table 1
Advantages and disadvantages of tripod polishing and focused ion beams TEM sample preparation methods when applied to porous thin films.

	Advantages	Disadvantages
Tripod polishing	Low running and material costs	Absence of in-situ control (blind process)
	Larger electron-transparent areas of homogeneous thickness: suitable for performing any (S) TEM study Easily adaptable and implementable to any lab	Possibility of specimen contamination during one of the preparation stages: promotion of unwanted oxidation of coatings
Focused ion beams	Straightforward, faster and cleaner	Sophisticated and expensive system which requires a high level of expertise Need for post-lift thinning to attain ultra-thin regions: Appearance of directional curtaining
	Selection of specific areas and particular orientations: In-situ control	Pt/C-layer protective layer can hinder subsequent analysis FIB-induced damage and ion implantation

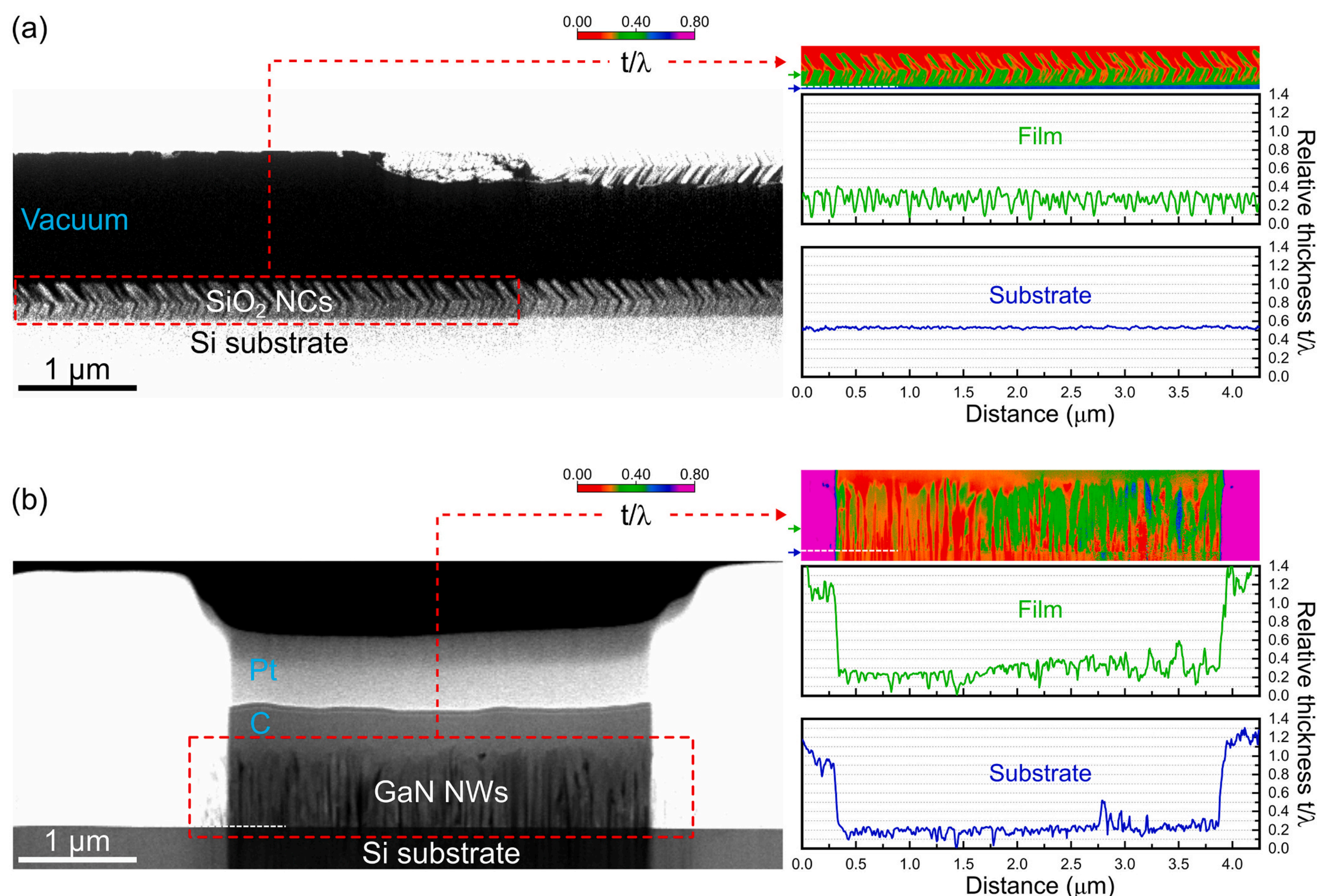

Fig. 3. Large field-of-view STEM-HAADF images and STEM-EELS thickness-map (over more than 4 μm width) of two porous films electron transparent cross-sections prepared by (a) tripod polishing and (b) FIB approaches. Note that intensity levels on the HAADF images were adjusted to see correctly the thinnest areas of interest in each sample. The film in (a) consists of a SiO_2 NCs bilayer deposited on a Si substrate by OAD (1st layer with $\alpha = 65°$, 2nd layer with $\alpha = 85°$). The film in (b) consists of a GaN NWs layer deposited on a Si substrate by MBE. The color maps represent the evolution of relative thickness (t/λ), where t is specimen thickness and λ is the characteristic mean free path for inelastic scattering (the same scale is used for comparison). Below the maps are shown t/λ profiles extracted across the substrate and across the layers (see small arrows on the left of each map to see the positions of the profile extraction).

electron mean free path of 90 nm in GaN). However, probably due to preferential milling artefacts arising from the uneven surface topography and porosity, thickness inhomogeneities both in the film and substrate regions are also evidenced (in some areas, larger and more fluctuating t/λ values around 0.4–0.6 are determined).

Thus, here is not only evidenced that the tripod polishing successes in preparing electron-transparent foils of porous multilayer systems with suitable thicknesses for HRTEM studies but also allows to obtain regions of uniform thickness extended to large areas, which make this kind of preparation the most suitable alternative when (S)TEM tomography or spectroscopy studies are needed. Besides, a specimen prepared by tripod polishing provides up to four regions of electron transparency which enables to explore larger sample areas. However, all the above mentioned is subject to certain limitations: although the tripod polishing procedure is well-defined, there are some factors that are going to influence the preparation of a particular specimen such as for instance the ability and care when dealing with the sample or the unique features of each film. This does not ensure that the result achieved through this method is always going to be the same but quite the opposite: both the aspect and the final thickness of the sample cannot be totally controlled in real time which can lead to situations in which the porous film subject to study is smashed, without knowing it, during one of the stages that tripod polishing implies or that, by strictly applying the method, the final thickness achieved for a sample is not the same as the one achieved for another of the same or different characteristics. In this sense, and for the purpose of making sure that a sample prepared by tripod polishing has not been significantly affected or damaged after the sample preparation process, an optional action could be to verify the prepared samples in a SEM microscope, verifying multiple samples at the same time and not individually since it could considerably increase the sample preparation costs and times (limited accessibility to SEM). In exchange, the tripod polishing weaknesses are precisely the strengths of the FIB preparation method, which is a process that allows a robust live control of the thickness and appearance of the TEM lamella. Moreover, the FIB method is the best alternative to prepare TEM lamellae of specific areas or orientations (which can be an issue of special interest when studying OAD coatings) with minimal damage and contamination, although, as seen before, it fails in its attempt to achieve homogeneous thicknesses after a final thinning at low energy. Likewise, it should not be neglected the effect of the protective layer of platinum deposited on the surface of a sample prior to FIB preparation (see Fig. 2 and Fig. 3(b)). Although the purpose of the Pt-layer is to protect the surface from incurring FIB induced damage, it can hinder subsequent analysis, especially on the surface. For instance, the appearance of unwanted peaks in spectroscopy which can hide or overlap relevant signals.

FIB-induced damage and ion implantation should also be addressed here, which both depend on preparation parameters like ion voltage, incident angle, substrate composition and ion species. In this sense,

conventional Ga^+ FIB processing is well known to produce amorphisation and Ga^+ implantation during FIB milling [71,72]. In this regard, some alternative solutions such as using low energy argon ion milling [73], Xe^+ PFIB systems [74,75], or focused-electron-beam-induced etching by chlorine [76] have been shown to be capable of removing Ga^+ implantation and amorphous damage from TEM specimens.

Another aspect to be taken into account is the budgetary limitations that a laboratory or research centre may have. The cost of a sophisticated FIB system implies an important investment that might not be assumable for all. In that case, tripod polishing postulates as the most affordable alternative to tackle the TEM specimen preparation of porous films due to its facility to be implemented in any laboratory without assuming a large investment. Likewise, it is interesting to highlight that, although it implies a higher cost of acquisition and commissioning, a FIB lamella provides much less areas of electron transparency that the one provided by a specimen prepared by tripod polishing.

Therefore, considering all the arguments previously referred, it is recommended, as a first approach, to address the preparation of nanostructured porous films by tripod polishing. On the other hand, the FIB preparation is only urged in the following cases: (i) when tripod polishing preparation fails; (ii) when the amount of material to be studied is so small that does not allow a tripod polishing preparation; (iii) when it is essential to reduce the presence of pollutants during preparation; (iv) to prepare specimens along particular orientations or specific areas; and (v) to prepare ultra-thin films for HRTEM observations when thickness non-uniformity does not undermine the studies to be performed.

3.2. Structure and morphology at micro- and nanoscale

Once established the most suitable routes to prepare electron-transparent foils of porous systems for TEM observations, the contribution that the application of each of the (S)TEM methods offer to the study of OAD and MBE nanowire porous nanostructures will be evaluated hereafter. In this sense, the capabilities of conventional transmission electron microscopy (CTEM) methods as a tool to explore the structure and morphology of such systems at different scales will first be explored.

After deposition, a widespread routine adopted by scientific

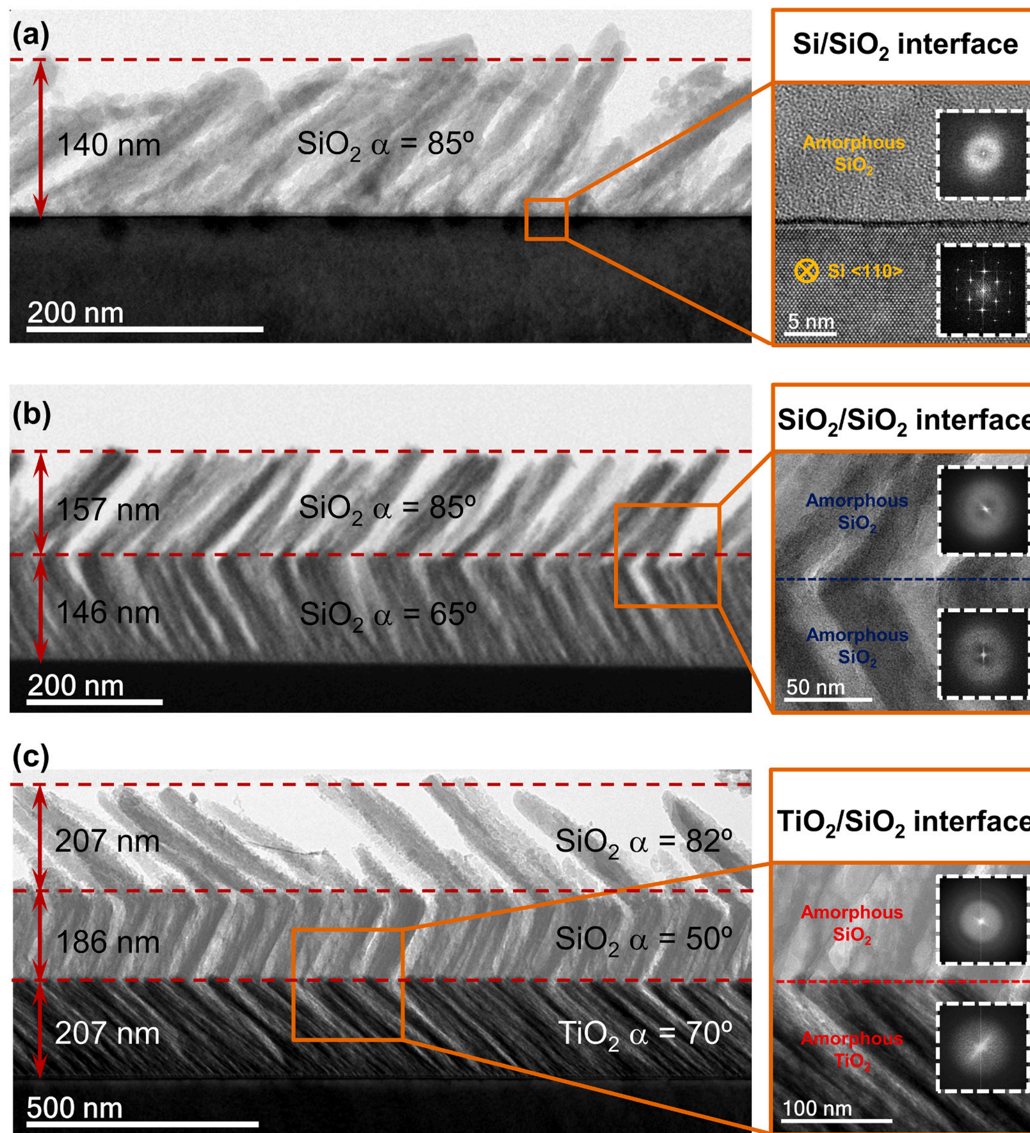

Fig. 4. Bright-field TEM overview of different OAD systems deposited on silicon substrates. (a) SiO_2 OAD monolayer deposited at $\alpha = 85°$. (b) SiO_2 OAD bilayer deposited at $\alpha = 65°$ and $\alpha = 85°$ with azimuthal rotation between the two layers of $\Phi = 180°$. (c) TiO_2/SiO_2 OAD trilayer deposited at α (TiO_2) = 70°, α (1st SiO_2) = 50° and α (2nd SiO_2) = 82° with azimuthal rotation between layers of $\Phi = 180°$. The insets of (a), (b) and (c) detail the features of the Si/SiO_2, SiO_2/SiO_2 and TiO_2/SiO_2 interfaces respectively, together with the corresponding FFT diffractogram of each layer.

community is to verify the overall look of the deposited nanostructure through SEM methods [15,20,22,50]. Even though the above could be considered as an appropriate preliminary approach, the comprehensive characterization of such morphologies and structures must be complemented by additional studies that allow to obtain, for instance, more detailed information on how the nanostructured film evolves as the deposition progresses or about how the transition between layers occurs. In this sense, TEM microscopy postulates as the most viable option because it is a very powerful and versatile tool that allows obtaining very valuable information for simulations [77] or providing new inputs to optical models [7].

Fig. 4 displays some bright-field (BF) TEM micrographs of different OAD mono-, bi- and trilayer systems, placing special emphasis on the aspect of the generated interfaces. It is worth to mention that all these specimens were prepared for TEM observations by means of tripod polishing. As can be seen, unlike SEM routines, TEM surveys not only allow to obtain general information about layer thicknesses and column tilt angles (β), but also allow to investigate how the transition between layers occurs or even determine the crystalline or amorphous nature of such porous coatings. In this sense, it is evidenced that the PVD-OAD deposition of SiO_2 and TiO_2 films gives rise to the generation of amorphous systems whose transitions between layers are characterised by being sharp and without generating intermixing layers, unlike what revealed in previous studies where an intermixing layer of about 50 nm thick was found at a Ge/MgF_2 interface [7]. Moreover, such micrographs also reveal that the tips of the lower columns behave as growth nuclei for the formation of new columns in upper layers.

Fig. 5 shows two bright-field TEM micrographs of IBS-OAD ITO films deposited at α = 85° using Xe and Ar ions. Note that, in this case, these TEM studies allowed to observe a great difference between the shape of the columns displayed in Fig. 5(a), which present a side sawtooth shape, and those found for the columns contained in Fig. 5(b), whose shapes are more regular. In view of the above, it can be assumed that such remarkable differences in the morphology of both systems must be closely linked to the nature of the ions sputtered during the deposition (Xe or Ar), which is in agreement with what was stated in a previous work in which it was determined that the selection of a particular sputtering ion has an effect not only on the overall nanostructure generated but also on the electro-optical properties of such ITO films [13].

On the other hand, studies of the structure and morphology of GaN nanowire films by means of CTEM methods can be also found in ref. [21]. All the examples provided until now have evidenced the ability of the TEM as a tool to inspect the structure and morphology of porous thin films with a great level of detail. Nevertheless, even though similar studies could have been performed by using a SEM microscope, these examples are just a small proof of all the possibilities that TEM microscopy can offer. In the following sections, the real potential of the TEM applied to the study of thin films will be revealed.

3.3. Crystal structure surveys

When a thin film presents a crystalline organization of its atoms, the orientation of its grains can determine the macroscopic properties of the system. These crystalline features are commonly explored by the scientific community through X-ray diffraction methods which allow to identify preferential crystal orientations or to determine the epitaxial alignment between the porous thin film and the underlying substrate

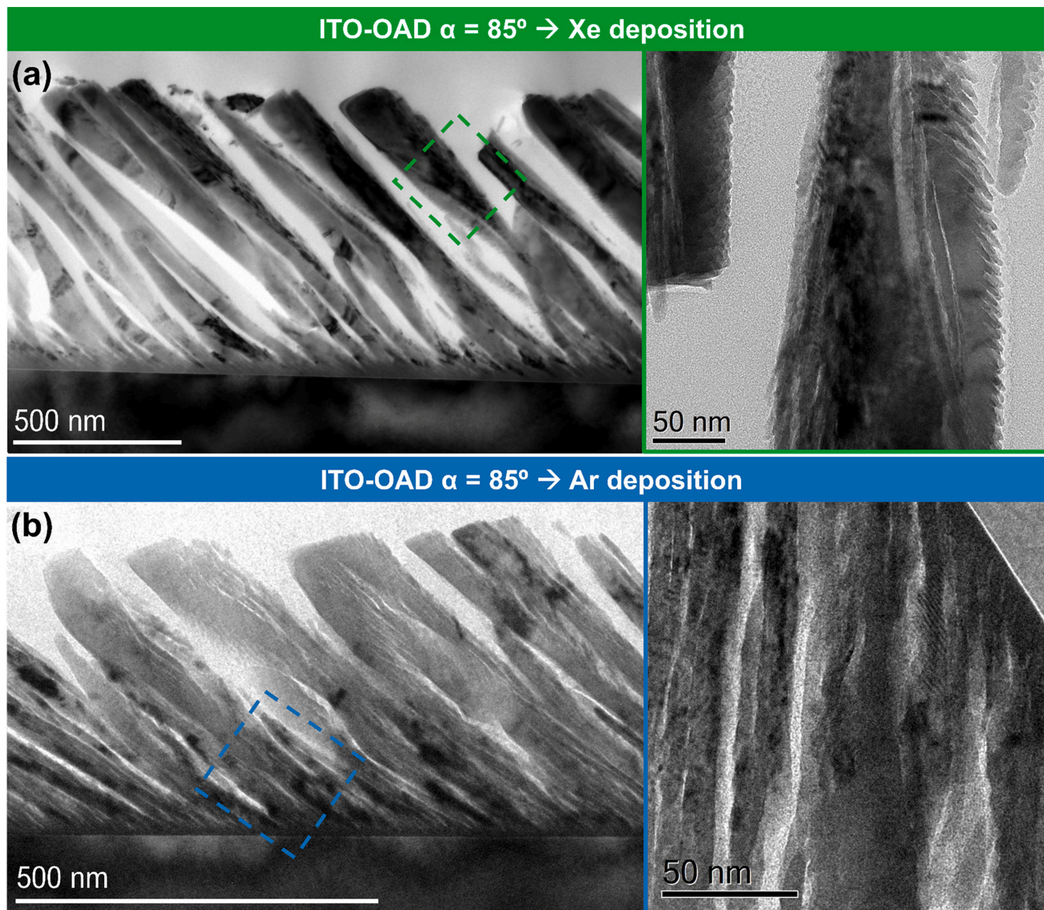

Fig. 5. Bright-field TEM overviews of ITO-OAD films prepared by (a) Xe and (b) Ar IBS at α = 85°. The insets place emphasis on the remarkable difference between the shape of the NCs generated as a function of the sputtered ion.

[78–81]. However, even though XRD studies normally provide overall diffraction statistics, which is especially suitable to study single crystalline systems, this technique does not allow to survey how the orientation of crystalline planes evolves along the layer thickness. This limitation can be overcome by combining high-resolution TEM (HRTEM) and selected area electron diffraction (SAED) methods, which not only allow to replicate the studies conducted by XRD but also to assess the crystal structure of a thin film locally. A preliminary proof of this can be found in ref. [21] in which the crystal structure of GaN nanowires as well as their epitaxial relationships were determined by combining HRTEM and SAED.

Another example of the validity and versatility of the TEM as a tool to carry out comprehensive structural characterizations of porous coatings at different levels is shown in Fig. 6 which reveals the nanostructural and crystallographic changes that an ITO OAD film (deposited by Xe IBS at $\alpha = 50°$) experiences along its layer thickness. On the one side, Fig. 6 (a) shows a remarkable difference between the nanostructure at the bottom part of the film, formed by bigger and more homogeneous grains, and some minor regions at the upper one, where arrays of slanted columns can be located (see the detail in Fig. 6(c) and (d)). Such study also reveals, thanks to HRTEM nanographs and FFT spectra performed at the top (Fig. 6(b)) and bottom (Fig. 6(d)) of the layer, the crystallographic changes that the ITO OAD film experiments along its layer thickness. These results are consistent with the assumptions reached in previous works, in which HRTEM images also revealed the presence of intragrain extended defects and dislocations at the top part of Ar-deposited IBS-OAD ITO films, underlining once again the remarkable difference between the films deposited with Ar (more subjected to backscattering and more energetic) and Xe ions [13]. In other words, the previous assumptions based on the division of the ITO OAD film into two layers of different morphology and crystallinity are here supported since, apart from the morphological differences aforementioned, a sharp switching in the preferential growth planes from (222) (bottom layer) to (440) (top layer) was evidenced as the film thickness increases for this specific deposition angle. This latter could also explain the significant difference between the optical and electrical behaviour of the upper region with respect to lower one. A complete study combining such structural TEM analyses with X-ray diffraction pole figure is currently in progress to understand the texture evolution of these ITO films with the deposition angle.

Before ending this section, it must be highlighted that atomic resolution TEM imaging can also be applied to figure out certain material properties. A clear example is polarity, which is an important feature, especially for III-nitrides such as GaN, since it has a significant effect on surface roughness [82] and reactivity [83,84], electron mobility [85,86] and dopant incorporation [87,88]. Many authors have examined the

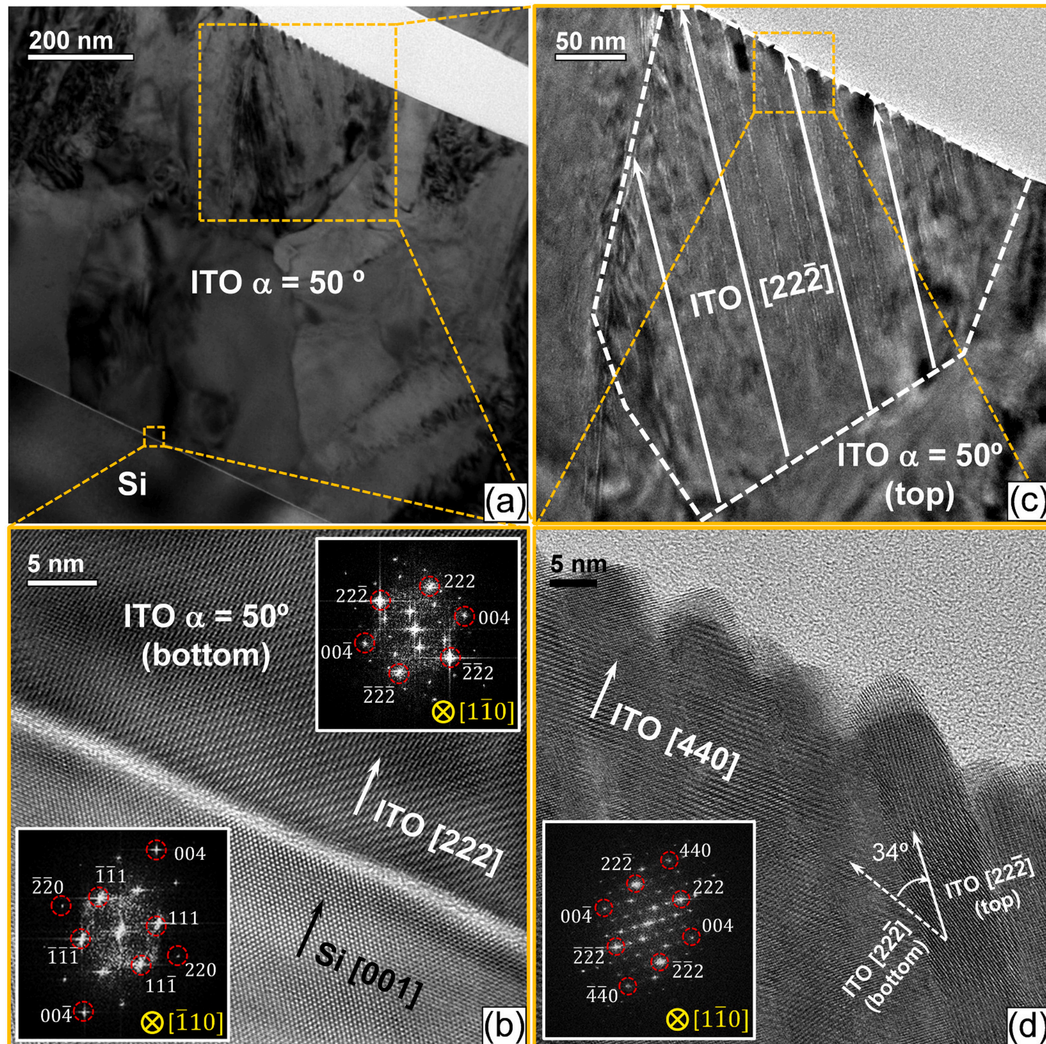

Fig. 6. Evolution of the crystallographic orientation of an ITO OAD film deposited by Xe IBS at $\alpha = 50°$. (a) Cross-section bright-field TEM overall observation of the ITO OAD film. (b) High-resolution TEM micrograph of the Si/ITO OAD interface with the corresponding FFT of each layer. (c) Bright-field TEM detail of the top part of the film. (d) High-resolution TEM micrograph of the top part of the film together with the associated FFT diffractogram of the region.

polarity of III-nitrides by wet etching [89], X-ray photoelectron diffraction [90], or using different TEM related techniques [91–97]. Among the TEM methods, aberration-corrected STEM combined with HAADF and annular bright field (ABF) has become one of the best strategies for directly displaying (not with the highest clarity for lighter atoms) the polarity of group III-nitride films manufactured in very different ways.

Fig. 7 illustrates an atomic resolution micrograph of a single crystalline GaN nanowire in [11$\bar{2}$0] orientation which was collected by means of a technique called integrated differential phase contrast STEM (iDPC-STEM) imaging [98–100] using an aberration corrected microscope. This recently introduced direct phase imaging technique allows to image the phase of the transmission function of a sample enabling live imaging of both light and heavy elements together at sub-Å resolution. This technique, which requires ultra-thin sample thicknesses and ultimate Cs-corrected microscopes to achieve good results, is especially favoured when applied to the study of porous thin films since they have, thanks to their large surface-to-volume ratio compared to their compact counterpart, more regions of optimal thickness which are located at the edges of such nanostructures. Accordingly, as displayed in Fig. 7, Gallium and Nitrogen dumbbells in GaN nanowire arrays were resolved thanks to the implementation of the iDPC-STEM technique, demonstrating the Ga-polarity of such nanostructures (Ga atoms on top of the double atom layers).

3.4. Chemical compositional analyses by imaging and spectroscopies

Until now, the potential and versatility of TEM methods to perform extensive structural characterizations of porous thin films at different levels has been solidly proved. Nevertheless, the capabilities and alternatives that the STEM mode offers for studying the chemical features of materials have not yet been fully explored.

On the one hand, when operating in STEM mode under dark field conditions, the image obtained using a HAADF detector will be due solely and exclusively to electrons that have been incoherently scattered from their path through matter at a sufficiently high angle. Since the HAADF detector is very sensitive to differences of the element irradiated based on the atomic number (*Z*-contrast), the resulting STEM-HAADF image will present an intensity approximately proportional to the square of the atomic number of the scanned region, as the heavier atoms will have a greater capacity to scatter electrons at higher angles due to bigger electrostatic interactions between their nuclei and the electron beam. This means that qualitative information about the chemical composition of a sample can be obtained, since the contrast in the HAADF images will be associated with a difference in the effective atomic number. Nonetheless, it must be considered that variations in thickness also significantly affect the intensity of the HAADF signal, which should be taken into account so as not to misinterpret the information contained in the HAADF image.

An example of this kind of studies can be seen in Fig. 8(a) which displays a STEM-HAADF micrograph conducted in a TiO_2/SiO_2 OAD trilayer system together with the HAADF signal profile acquired along individual columns belonging to each of the layers. As can be appreciated, the HAADF signal becomes more intense in the TiO_2 layer (brighter contrast) than in both SiO_2 layers, which is, in principle, reasonable since titanium (Z = 22) has a greater atomic number than silicon (Z = 14). Moreover, the HAADF profile reveals a very similar HAADF intensity for both SiO_2 layers compared to the one recorded for the TiO_2 layer, which also suggests that the thickness of the thinned TEM sample is quite homogeneous (note that this sample was prepared for TEM observations by tripod polishing). In this sense, it is worth mentioning

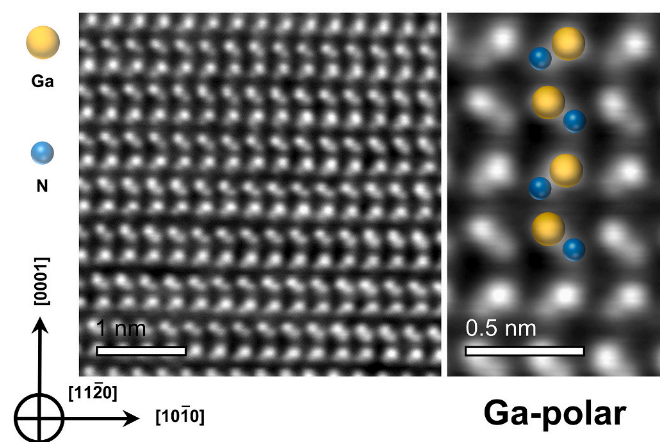

Fig. 7. iDPC-STEM image of a single crystalline GaN nanowire along the [11$\bar{2}$0] zone axis. Beam current was maintained below 30 pA, the dwell time is 5 μs, beam convergence angle is 21.4 mrad and the field of view is 12.6 nm. The resulting range of collection angles for the annular DF detector (DF4) is 15–57 mrad, with DPC and scan rotations of 8° and − 3°, respectively. Note that the image is shown as it appears live on the screen without any post-processing. The image reveals the larger Ga atoms on top of the double atom layers (Ga-polar).

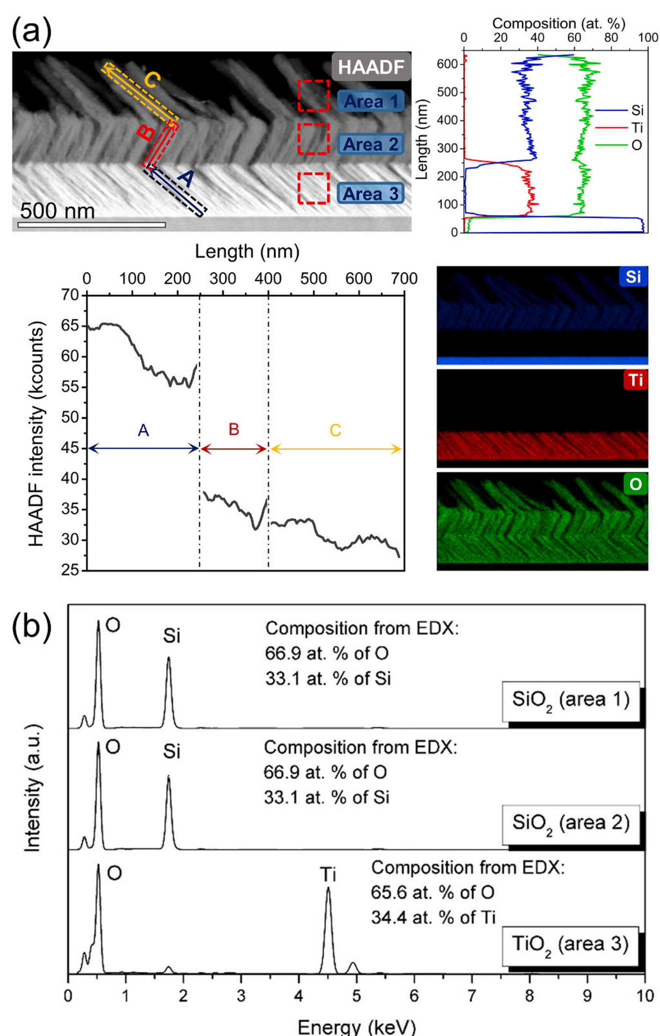

Fig. 8. STEM-EDX analysis of a TiO_2/SiO_2 OAD trilayer deposited at α (TiO_2) = 70°, α (1st SiO_2) = 50° and α (2nd SiO_2) = 82° with azimuthal rotation between layers of Φ = 180°. (a) STEM-HAADF micrograph and elemental maps obtained for Si, Ti and O atoms together with the elemental profiles along the whole coating thickness and the HAADF profile collected along individual columns of each layer. (b) EDX integrated spectra and associated compositional quantitative analysis for each OAD layer.

that this same STEM imaging technique was implemented in previous studies to identify hollow and solid GaN nanowires thanks to the fact that the HAADF intensity is also proportional to the quantity of projected material (see ref. [21]).

Nevertheless, what really makes the TEM a very powerful analytic tool is the combination of STEM imaging and spectroscopy. In this sense, the most common TEM-based spectroscopy techniques are Energy Dispersive X-ray Spectroscopy (EDX or EDS) and Electron Energy Loss Spectroscopy (EELS). Based on X-rays emitted as a result of the interaction of the primary electron beam with the atoms that constitute a material, the EDX technique allows to identify and quantify the elemental constituents of a sample by the analysis of the resulting X-ray energies which are characteristic of specific elements. This analytical technique is especially useful when is applied to the study of porous thin films since not only allows to uncover, by means of spectrum images (SIs), the quantitative distribution of the elements that compose a sample but also to know additional relevant information like how the interfaces are developed [7] or if the porous nanostructure is subjected to the spontaneous oxidation of its exposed surfaces [12,14].

An evidence of the capability of this analytical tool is presented in Fig. 8, in which the EDX elemental maps and profiles of a TiO_2/SiO_2 OAD trilayer (Fig. 8(a)) are displayed together with the EDX integrated spectra and associated atomic quantifications of each layer (Fig. 8(b)). EDX spectra were recorded over 100×100 nm^2 areas and large integration times (several minutes, collecting a total of 1137 frames) using current probes of about 450 pA, beam convergence angles of 16 mrad, dwell times of 5 μs and dispersions of 5 eV/channel over 4000 channels. The FEI Velox™ software was used for STEM-EDX data acquisition and processing. EDX elemental quantifications of TiO_2 and SiO_2 OAD layers were performed by using the standardless method (i.e. based on theoretical sensitivity factors). Although the accuracy of this approach is rarely considered better than 10% [101], especially for low Z elements like O, the measurement uncertainties attained here (below 5%) support the validity of the standardless quantification since the atomic proportions obtained are very close to the ideal stoichiometry (66.9 at. % of O, 33.1 at. % of Si for SiO_2 layers; 65.6 at. % of O, 34.4 at. % of Ti for TiO_2 layer). Additionally, it should be also noted that the combination of EDX elemental maps and profiles (Fig. 8(a)) also provides valuable information on how the transition between layers takes place (intermixing thickness, composition, etc.).

On the other hand, another alternative way to carry out elemental quantifications at nanometer scale consists of measuring the loss of energy from the inelastic interactions between the electron beam and a thin specimen. That loss of energy will be associated with different characteristic electronic transitions of the constituent elements of a sample, allowing their identification and quantification. This is the basis of the EELS technique which, compared to EDX, provides improved signal, spatial resolution, energy resolution and sensitivity for low atomic number elements [101,102]. In addition to the above-mentioned, EELS information can also be used to characterize chemical bonding configurations, oxidation states, valence and conduction band electronic properties or even sample thickness (see Fig. 3). Special mention must be made of the low-loss EELS region, which not only contains valuable information about the chemical composition and electronic structure but also about the optical properties of a specimen, opening an alternative way to locally probe the optical behaviour of porous thin films. Taking advantage of such capacities, EELS analysis were conducted in previous works not only for the sake of demonstrating the formation of core-shell-type nanostructures in Ge OAD layers as a consequence of the spontaneous surface oxidation of such porous architectures but also for determining the oxidation state of the oxide generated in the same way as XPS surveys (see ref. [12]). Likewise, it is worth mentioning that similar local STEM-EELS analysis were also performed on IBS-OAD ITO films with the aim of examining the distribution of In, Sn and O along the diameter of such ITO nanocolumns. However, the overall overlapping of the EELS signals coming from the different elements and compounds made the obtained results inconclusive.

Ultimately, in order to illustrate the possibilities offered by (S)TEM techniques to solve problems related to the composition of nanostructured porous films, STEM-EDX and EELS analytical methods were applied on a GaN NWs film system prepared by FIB (see Fig. 3(b)) and compared. For that, the STEM mode (convergence angle of 10.5 mrad, probe current of ~150 pA) was used in a FEI Talos F200X G2 fitted with a Gatan Imaging Filter (GIF) continuum spectrometer and Super-X energy-dispersive X-ray spectrometry system that includes four silicon drift detectors.

On the one hand, core-loss EELS spectrum images (SI) including the N—K and Ga-L edges were acquired over the whole GaN NWs film using a 40.4 mrad collection angle, a dispersion of 0.75 eV/channel, a pixel step of 10 nm and an exposure time of 0.25 s/pixel (Fig. 9(a)). As thin and uniformly-thick specimen areas are generally required for accurate EELS analysis, the t/λ map was used as a reference (see Fig. 3(b)). A thin enough region ($t/\lambda \leq 0.3$) was selected to reasonably neglect multiple scattering effects for further quantification (for this reason, no deconvolution with the low-loss signal was applied in that case). Beside the expected N—K and Ga-L edges observed at about 401 eV and 1115 eV, respectively, the presence of a noticeable O—K edge signal (see EELS spectrum on top of Fig. 9(a)) suggests that the NWs are partly oxidized. More details about the composition of these nanostructures have been obtained from quantitative elemental analyses of the EELS data, which was carried out using the implemented routine in the Gatan Digital Micrograph software. In order to measure the atomic concentrations ratios of Ga, N and O, a great care was taken in the signal extraction using suitable power-law models to remove the background below each edge (see extraction on EELS spectrum in Fig. 9(a)). The element ratio technique was then applied using a 50 eV-width window to determine the integral intensities and to calculate the ionization cross-sections of each edge (according to ref. [102], the hydrogenic model was used for cross-sections). Quantification over a 100×100 nm^2 area across one individual NW confirms that the average Ga:N ratio is close to 1:1 (see Table 2), which is fully consistent with the wurtzite nanowire lattices evidenced through HRTEM [21]. It also reveals that an amount of ~9% is trapped within the NWs. The 2D elemental maps and profiles show that despite this composition is maintained over the whole film thickness, a significant accumulation of O and Ga and a drop of N amount at the border of the NWs occur, which could be related to surface oxidation of these high surface-to-volume ratio structures due to air exposure, as supposed in a previous work [14].

To confirm those results, it is insightful to compare them to elemental measurements that can be obtained by STEM-EDX (Fig. 9(b)), which appears as an alternative technique to obtain spatially-resolved compositional information. For comparison purpose, an area with similar characteristics than for STEM-EELS (similar field of view, same specimen thickness $t/\lambda \approx 0.3$) was studied by EDX using the Velox interface. For acquisition, a pixel step of 4.4 nm and a dwell time of 100 μs/pixel were set, and the signal was integrated over 220 frames. In the same way as for EELS, the EDX spectra across the NWs present lines of Ga, N and O, but also Cu signals due to the lamella supporting grid. To determine the relative composition of Ga, N and O, the background of the EDX spectra was removed and a full standardless quantification with the Brown-Powell ionization cross-section model was performed using the K-lines of Ga, N and O. To improve the quantification, deconvolution of the Cu peaks was applied and the K-line of Ga was preferred to L-line to avoid contributions from overlapping peaks. In the present case, compositional results obtained by EDX are very similar to those achieved by EELS (see Table 2 and Fig. 9), suggesting that both techniques are suitable for spatially resolved compositional analyses of nanostructured porous films.

Nevertheless, in many cases, depending on many factors such as the type of material or the thickness of the lamella and its sensitivity to electron beam, EELS or EDX should be preferred for elemental analysis.

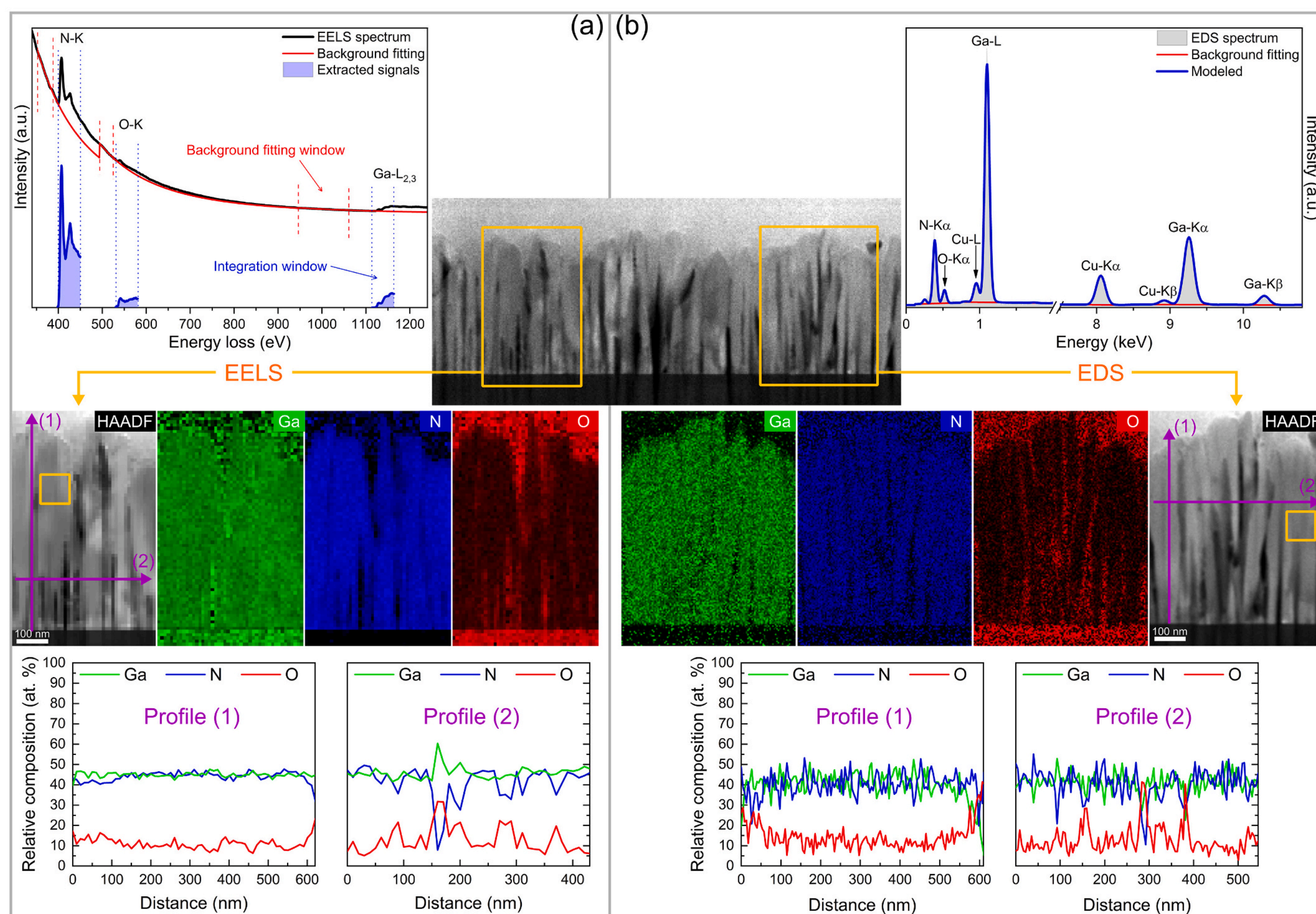

Fig. 9. (a) STEM-EELS and STEM-EDX spectrum image datasets recorded across GaN NWs (using drift correction). The integrated spectra over 100 × 100 nm^2 areas (indicated on the HAADF images below by yellow rectangles), and the extracted/modelled signals used for quantifications are shown on the top. The quantification results in the square areas are reported in Table 2. The Ga, N, and O 2D concentration maps obtained after quantifications as well as the corresponding HAADF images of the analysed regions are displayed in the middle. Longitudinal (1) and transversal (2) concentration profiles extracted from the 2D maps are plotted at the bottom. (For interpretation of the references to color in this figure legend, the reader is referred to the web version of this article.)

Table 2
Relative elemental compositions obtained in a 100 × 100 nm^2 area across one single NW determined by EELS and EDX quantification. Errors in EELS quantification are assumed to be 5% due to uncertainties in cross-sections according to ref. [103]. Errors in EDX quantification are directly provided by the Velox software.

Analysis method	Ga (at. %)	N (at. %)	O (at. %)
EELS	45 ± 3	47 ± 3	9 ± 1
EDX	44 ± 9	48 ± 8	8 ± 3

We must be aware that neither of these two techniques is better than the other, and that they must rather be seen as complementary, each with their strengths and weaknesses (as summarized in Table 3). In a nutshell, the strengths of EELS are (i) its capacity to provide extra information (like chemical bonding electron-loss near edge structure, excitation of valence band electrons, electronic structure and thickness) that EDX cannot, and that are now achievable simultaneously using DualEELS capabilities; (ii) its better elemental detection capacities which allow faster acquisition, better resolution, use of lower current to avoid beam damage and stronger sensitivity to light elements; (iii) its better accuracy. However, to take the full benefit of this technique and ensure reliable quantifications, important requirements must be fulfilled: this includes working with very thin specimen ($t/\lambda \leq 0.3$), knowing very well the experimental setup (including convergence and collection angles), and spend time to process carefully the data. The clear advantages of the EDX are (i) its greater ease of use both at the experimental and post-processing level, and (ii) its lower limitations regarding the specimen thickness requirements. It is important to note that the recent implementation of silicon-drift detector (SDD) has made it possible to substantially increase the elemental detection, including light elements.

Table 3
Strengths (+) and limitations (−) for STEM-EELS and EDX analytical methods.

		EELS	EDS
Analytical capabilities	Elemental information	+	+
	Chemical fingerprinting	+	−
	Additional capabilities (valence/conduction electron density, thickness measurement, band structure and interband transitions)	+	−
Detection	Signal collection	+	−
	Energy resolution	+	−
	Sensitivity to light elements	+	−
	Sensitivity to heavy elements	−	+
Acquisition	Fast acquisition	+	−
	Simplicity	−	+
	Live visualization	−	+
Elemental quantification	Dependence to experimental setup	−	+
	Requirement of very thin specimen	−	+
	Complexity of data processing	−	+
	Accuracy	+	−

3.5. 3D reconstructions: STEM-HAADF tomography

Electron Tomography (ET) is a technique that allows to reconstruct the three-dimensional structure of a specimen from a set of two-dimensional images recorded at various tilt angles (tilt-series) which are then processed off-line using different reconstruction algorithms [104–109]. Among the different ET variants, STEM tomography has become established as one of the most powerful. As 3D characterizations at the nanoscale represent valuable insights into the design of nanomaterials, STEM tomography examinations of thin films are becoming increasingly popular for material scientists, being the HAADF signal preferred to BF because of its monotonic dependence on the sample thickness [110,111]. Applied to the characterization of porosity-controlled thin films, STEM-HAADF tomography reconstructions can supply relevant geometric features (3D morphologies and textures, distribution and interaction between nanostructures, porosity profiles, anisotropy, etc.) which will enable a better understanding of how growth events occur as well as evaluate the influence they have on the properties of the coating.

Fig. 10(a) displays the STEM-HAADF electron tomography 3D reconstruction of a TiO_2/SiO_2 OAD trilayer system together with the extracted porosity profile along the surface normal (Fig. 10(b)). For a detailed description of the experimental data acquisition, segmentation, 3D reconstruction, and porosity profile extraction, refer to Supplementary Material Section I. According to the literature, needle-geometry samples accomplished by focused ion beams have been proved to be the most suitable approach for TEM tomographic experiments, since this geometry prevents thickness changes when tilting the sample [112]. Nonetheless, the good appearance of the 3D reconstruction presented here also suggests that tripod polishing is also a suitable approach to handle STEM tomography examinations. Note how the top views reveal the remarkable porosity and morphological texture changes when moving from one layer to another. Moreover, it must be highlighted that the information extracted from ET reconstructions not only provides additional insights into the nanostructure but also very useful inputs such as the porosity profile which can be used to describe the optical behaviour of a system. Good proof of this is reported in some of our previous works in which the 3D volume reconstructions of several porous films allowed us to assess the scattering behaviour of antireflective coatings by means of finite-difference time domain (FDTD) simulations (see ref. [9]) as well as to validate and improve optical models by implementing the porosity profiles extracted from STEM-HAADF tomographic reconstructions into ellipsometry effective-medium approximation models (see ref. [8] and ref. [14]).

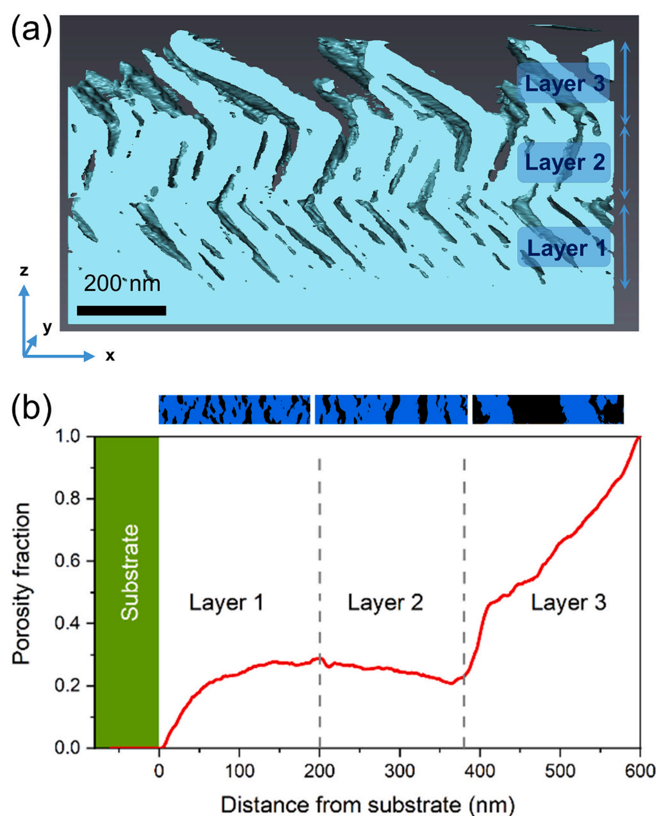

Fig. 10. (a) STEM-HAADF 3D reconstruction of a TiO_2/SiO_2 OAD trilayer. (b) Associated porosity profile extracted along the surface normal, together with some representative planar views of each layer obtained by data segmentation (voids are shown in black colours).

4. Conclusions

In this work, the possibilities and alternatives offered by the application of (S)TEM methods for a comprehensive and exhaustive characterization of porous nanostructured coatings were assessed. After identifying the tricky collection of porous TEM lamellae as one of the main reasons for the absence of advanced (S)TEM characterizations of such systems, two different TEM sample preparation strategies were tested. In this sense, both tripod polishing and focused ion beams were evidenced to be suitable approaches for preparing electron-transparent foils of porous thin films. Likewise, a comparative analysis on the most appropriate sample preparation option as a function of the (S)TEM study to be conducted was also met. Once this difficulty was overcome, several (S)TEM characterization techniques, such as HRTEM, SAED, STEM-HAADF, STEM-iDPC, STEM-EDX, STEM-EELS or ET, were implemented on several OAD and NW porous films. In this way, the implementation of new breakthroughs in (S)TEM imaging and spectroscopy allowed us to accomplish some of the pioneering studies presented here, highlighting the versatility and capabilities that TEM methods offer to the extensive characterization of porous nanostructures. Issues, such as (a) the morphology, porosity, crystal structure and composition of individual columns or nanowires, local regions and entire layers; (b) the nature, morphology, composition and thickness of transitions between layers; and (c) the 3D reconstruction of such porous structures were finely explored by (S)TEM methods, providing, at the same time, both local and overall data. Note that the above is not achieved by means other characterization techniques such as XPS, which only provides quantitative information about the first 1–5 nm thick of a sample, or XRD, which only gives global information, which may lead to an incomplete or misleading characterization of the coating. Furthermore, it was also emphasized the valuable contribution of TEM studies for the optical and electrical characterization of such porous systems especially when combined with other techniques like spectrophotometric and Hall effect measurements and, particularly, spectroscopy ellipsometry.

Based on the evidences shown throughout this work, it is intended to make materials scientists aware of the niche of opportunity that (S)TEM methods represent for the advanced characterization of porous nanostructured systems, opening new horizons, since they allow to examine the structure and composition of materials at scales and levels of detail that other techniques do not reach, simplifying methodologies, as they allows to obtain, by using a single equipment, equivalent results to those that could be acquired thorough the combination of SEM, AFM, XPS and XRD analysis, and contributing to a better knowledge of growth mechanisms and properties.

Author contributions

The manuscript was written through contributions of all authors. All authors have given approval to the final version of the manuscript.

Data availability

The raw/processed data required to reproduce these findings cannot be shared at this time due to technical or time limitations.

Declaration of Competing Interest

None.

Acknowledgments

The authors would like to express their gratitude to Ellen Backen, applications scientist from Thermo Fisher Scientific, for the FIB samples prepared at the Scios 2 HiVac system at Nanoport (Eindhoven). A. J. Santos would like to thank the IMEYMAT Institute and the Spanish Ministerio de Educación y Cultura for the concessions of grants (ICARO-173873 and FPU16-04386). The "Talent Attraction Program" of the University of Cádiz is acknowledged by supporting B. Lacroix contract code E-11-2017-0117214. University of Cádiz and IMEYMAT are also agreed by financing the mutual facilities available at the UCA R&D Central Services (SC-ICYT), the UCA project reference "PUENTE PR2018-040", and the IMEYMAT project references "AGREGADOR 2018-1" and "LÍNEAS PRIORITARIAS PLP2019120-3". The authors would like to acknowledge the financial support provided by Sêr Cymru National Research Network in Advanced Engineering and Materials. This work was also partly carried out in the framework of the associate laboratory PRIMEO ("Partnership for Research and Innovation in Emerging Materials for phOtonics") between Safran Electronics & Defense and PPRIME Institute. It benefited from the partial support of the DGA (Direction Générale de l'Armement, the French Defense Procurement Agency), the "Nouvelle Aquitaine" Region and the European Structural and Investment Funds (ERDF reference P-2016 BAFE-209): IMATOP project.

Appendix A. Supplementary data

Three-dimensional STEM-HAADF tomography reconstructions (experimental data acquisition; segmentation; 3D reconstruction; and porosity profile extraction) (PDF). Supplementary data to this article can be found online at https://doi.org/10.1016/j.matchar.2022.111741.

References

[1] J.M. Albella, Capas delgadas y modificación superficial de materiales, Consejo Superior de Investigaciones Científicas, 2018.
[2] J.P. Davim, Materials and Surface Engineering: Research and Development, Woodhead Publishing, 2012.
[3] X.J. Li, Z. Wei Song, Y. Zhao, Y. Wang, X.C. Zhao, M. Liang, W.G. Chu, P. Jiang, Y. Liu, Vertically porous nickel thin film supported Mn_3O_4 for enhanced energy storage performance, J. Colloid Interface Sci. 483 (2016) 17–25, https://doi.org/10.1016/j.jcis.2016.08.006.
[4] E. Dislaki, S. Robbennolt, M. Campoy-Quiles, J. Nogués, E. Pellicer, J. Sort, Coercivity modulation in Fe–cu pseudo-ordered porous thin films controlled by an applied voltage: a sustainable, energy-efficient approach to magnetoelectrically driven materials, Adv. Sci. 5 (2018) 1800499, https://doi.org/10.1002/advs.201800499.
[5] A. Dubey, S.K. Kolekar, E.S. Gnanakumar, K. Roy, C.P. Vinod, C.S. Gopinath, Porous thin films toward bridging the material gap in heterogeneous catalysis, Catal. Struct. React. 2 (2016) 1–12, https://doi.org/10.1080/2055074X.2015.1133269.
[6] S. Abate, G. Centi, S. Perathoner, F. Frusteri, Enhanced stability of catalytic membranes based on a porous thin Pd film on a ceramic support by forming a Pd-ag interlayer, Catal. Today 118 (2006) 189–197, https://doi.org/10.1016/j.cattod.2005.12.008.
[7] F. Maudet, B. Lacroix, A.J. Santos, F. Paumier, M. Paraillous, C. Dupeyrat, R. García, F.M. Morales, T. Girardeau, Towards perfect MWIR transparency using oblique angle deposition, Appl. Surf. Sci. 470 (2019) 943–950, https://doi.org/10.1016/j.apsusc.2018.11.176.
[8] F. Maudet, B. Lacroix, A.J. Santos, F. Paumier, M. Paraillous, S. Hurand, A. Corvisier, C. Marsal, B. Giroire, C. Dupeyrat, R. García, F.M. Morales, T. Girardeau, Optical and nanostructural insights of oblique angle deposited layers applied for photonic coatings, Appl. Surf. Sci. 520 (2020) 146312, https://doi.org/10.1016/j.apsusc.2020.146312.
[9] F. Maudet, B. Lacroix, A.J. Santos, F. Paumier, M. Paraillous, S. Hurand, A. Corvisier, C. Dupeyrat, R. García, F.M. Morales, T. Girardeau, On the importance of light scattering for high performances nanostructured antireflective surfaces, Acta Mater. 188 (2020) 386–393, https://doi.org/10.1016/j.actamat.2020.02.014.
[10] C. Toccafondi, S. Uttiya, O. Cavalleri, G. Gemme, E. Barborini, F. Bisio, M. Canepa, Optical properties of nanogranular and highly porous TiO_2 thin films, J. Phys. D. Appl. Phys. 47 (2014) 485301, https://doi.org/10.1088/0022-3727/47/48/485301.
[11] J. Prikulis, T. Tamulevičius, R. Poplausks, G. Bergs, I. Apsite, U. Malinovskis, A. Actins, D. Erts, Optical properties of thin metal films with nanohole arrays on porous alumina-aluminum structures, RSC Adv. 5 (2015) 68143–68150, https://doi.org/10.1039/c5ra12880c.
[12] A.J. Santos, B. Lacroix, F. Maudet, A. Corvisier, F. Paumier, C. Dupeyrat, T. Girardeau, R. García, F.M. Morales, Surface oxidation of amorphous Si and Ge slanted columnar and mesoporous thin films: evidence, scrutiny and limitations for infrared optics, Appl. Surf. Sci. 493 (2019) 807–817, https://doi.org/10.1016/j.apsusc.2019.07.064.
[13] B. Lacroix, A.J. Santos, S. Hurand, A. Corvisier, F. Paumier, T. Girardeau, F. Maudet, C. Dupeyrat, R. García, F.M. Morales, Nanostructure and physical properties control of indium tin oxide films prepared at room temperature through ion beam sputtering deposition at oblique angles, J. Phys. Chem. C 123 (2019) 14036–14046, https://doi.org/10.1021/acs.jpcc.9b02885.
[14] A.J. Santos, B. Lacroix, E. Blanco, S. Hurand, V.J. Gómez, F. Paumier, T. Girardeau, D.L. Huffaker, R. García, F.M. Morales, Simultaneous optical and electrical characterization of GaN nanowire arrays by means of Vis-IR spectroscopic ellipsometry, J. Phys. Chem. C 124 (2020) 1535–1543, https://doi.org/10.1021/acs.jpcc.9b10556.
[15] M.M. Hawkeye, M.J. Brett, Glancing angle deposition: Fabrication, properties, and applications of micro- and nanostructured thin films, J. Vac. Sci. Technol. A Vacuum, Surfaces, Film 25 (2007) 1317, https://doi.org/10.1116/1.2764082.
[16] H. van Kranenburg, C. Lodder, Tailoring growth and local composition by oblique-incidence deposition: a review and new experimental data, Mater. Sci. Eng. R 11 (1994) 295–354, https://doi.org/10.1016/0927-796X(94)90021-3.
[17] K. Robbie, M.J. Brett, Sculptured thin films and glancing angle deposition: growth mechanics and applications, J. Vac. Sci. Technol. a-Vacuum Surfaces Film. 15 (1997) 1460–1465, https://doi.org/10.1116/1.580562.
[18] M.M. Hawkeye, M.T. Taschuk, M. Brett, Glancing Angle Deposition of Thin Films, Wiley, 2014.
[19] Y. He, Y. Zhao, Advanced multi-component nanostructures designed by dynamic shadowing growth, Nanoscale. 3 (2011) 2361, https://doi.org/10.1039/c1nr10103j.
[20] A. Barranco, A. Borras, A.R. Gonzalez-Elipe, A. Palmero, Perspectives on oblique angle deposition of thin films: from fundamentals to devices, Prog. Mater. Sci. 76 (2016) 59–153, https://doi.org/10.1016/j.pmatsci.2015.06.003.
[21] V.J. Gómez, A.J. Santos, E. Blanco, B. Lacroix, R. García, D.L. Huffaker, F. M. Morales, Porosity control for plasma-assisted molecular beam epitaxy of GaN nanowires, Cryst. Growth Des. 19 (2019) 2461–2469, https://doi.org/10.1021/acs.cgd.9b00146.
[22] P. Tyagi, C. Ramesh, B.S. Yadav, S.S. Kushvaha, M.S. Kumar, Laser molecular beam epitaxy of vertically self-assembled GaN nanorods on ta metal foil: role of growth temperature and laser repetition rate, CrystEngComm. 21 (2019) 5448–5454, https://doi.org/10.1039/c9ce00855a.
[23] R. Sun, G.G. Wang, Z.C. Peng, Fabrication and UV photoresponse of GaN nanowire-film hybrid films on sapphire substrates by chemical vapor deposition method, Mater. Lett. 217 (2018) 288–291, https://doi.org/10.1016/j.matlet.2018.01.107.
[24] H.G. Cha, C.W. Kim, Y.H. Kim, M.H. Jung, E.S. Ji, B.K. Das, J.C. Kim, Y.S. Kang, Preparation and characterization of α-Fe_2O_3 nanorod-thin film by metal-organic chemical vapor deposition, Thin Solid Films 517 (2009) 1853–1856, https://doi.org/10.1016/j.tsf.2008.10.023.
[25] J.Q. Xi, M.F. Schubert, J.K. Kim, E.F. Schubert, M. Chen, S.Y. Lin, W. Liu, J. A. Smart, Optical thin-film materials with low refractive index for broadband elimination of Fresnel reflection, Nat. Photonics 1 (2007) 176–179, https://doi.org/10.1038/nphoton.2007.26.
[26] S.R. Kennedy, M.J. Brett, Porous broadband antireflection coating by glancing angle deposition, Appl. Opt. 42 (2003) 4573–4579, https://doi.org/10.1364/AO.42.004573.
[27] L. Tian, L. Li, C. Ban, M. Wu, Fabrication and characterization of TiO_2 antireflection coatings with gradient-index, in: 2017 IEEE 12th International Conference on Nano/Micro Engineered and Molecular Systems (NEMS), 2017, pp. 131–136, https://doi.org/10.1109/NEMS.2017.8016990.
[28] C.-H. Chang, J.A. Dominguez-Caballero, H.J. Choi, G. Barbastathis, Nanostructured gradient-index antireflection diffractive optics, Opt. Lett. 36 (2011) 2354, https://doi.org/10.1364/ol.36.002354.
[29] R. Alvarez, J.M. Garcia-Martin, A. Garcia-Valenzuela, M. Macias-Montero, F. J. Ferrer, J. Santiso, V. Rico, J. Cotrino, A.R. Gonzalez-Elipe, A. Palmero, Nanostructured Ti thin films by magnetron sputtering at oblique angles, J. Phys. D. Appl. Phys. 49 (2016), 045303, https://doi.org/10.1088/0022-3727/49/4/045303.
[30] R. El Beainou, N. Martin, V. Potin, P. Pedrosa, M.A.P. Yazdi, A. Billard, Correlation between structure and electrical resistivity of W-cu thin films prepared by GLAD co-sputtering, Surf. Coatings Technol. 313 (2017) 1–7, https://doi.org/10.1016/j.surfcoat.2017.01.039.

[31] H. Chu, S. Song, C. Li, D. Gibson, Surface enhanced Raman scattering substrates made by oblique angle deposition: methods and applications, Coatings. 7 (2017) 26, https://doi.org/10.3390/coatings7020026.

[32] R.K. Jain, Y.K. Gautam, V. Dave, A.K. Chawla, R. Chandra, A study on structural, optical and hydrophobic properties of oblique angle sputter deposited HfO_2 films, Appl. Surf. Sci. 283 (2013) 332–338, https://doi.org/10.1016/j.apsusc.2013.06.112.

[33] A. Esfandiar, H. Savaloni, F. Placido, On the fabrication and characterization of graded slanted chiral nano-sculptured silver thin films, Phys. E Low-Dimensional Syst. Nanostructures. 50 (2013) 88–96, https://doi.org/10.1016/j.physe.2013.03.002.

[34] S. Larson, Y. Zhao, Tuning the composition of Bi_xW_yO nanorods towards zero bias PEC water splitting, Nanotechnology. 27 (2016) 255401, https://doi.org/10.1088/0957-4484/27/25/255401.

[35] A.R. Shetty, A. Karimi, Texture mechanisms and microstructure of biaxial thin films grown by oblique angle deposition, Phys. Status Solidi Basic Res. 249 (2012) 1531–1540, https://doi.org/10.1002/pssb.201248010.

[36] D.B. Polat, O. Keles, K. Amine, Well-aligned, ordered, nanocolumnar, cu-Si thin film as anode material for lithium-ion batteries, J. Power Sources 270 (2014) 238–247, https://doi.org/10.1016/j.jpowsour.2014.07.087.

[37] P. Salazar, V. Rico, A.R. González-Elipe, Non-enzymatic hydrogen peroxide detection at NiO nanoporous thin film- electrodes prepared by physical vapor deposition at oblique angles, Electrochim. Acta 235 (2017) 534–542, https://doi.org/10.1016/j.electacta.2017.03.087.

[38] Z.L. Wang, Picoscale science and nanoscale engineering by electron microscopy, J. Electron Microsc. 60 (2011) 269–278, https://doi.org/10.1093/jmicro/dfr027.

[39] G. McMullan, A.R. Faruqi, D. Clare, R. Henderson, Comparison of optimal performance at 300keV of three direct electron detectors for use in low dose electron microscopy, Ultramicroscopy. 147 (2014) 156–163, https://doi.org/10.1016/j.ultramic.2014.08.002.

[40] F. Hosokawa, H. Sawada, Y. Kondo, K. Takayanagi, K. Suenaga, Development of Cs and cc correctors for transmission electron microscopy, J. Electron Microsc. 62 (2013) 23–41, https://doi.org/10.1093/jmicro/dfs134.

[41] W. Phae-ngam, M. Horprathum, C. Chananonnawathorn, T. Lertvanithphol, B. Samransuksamer, P. Songsiririthigul, H. Nakajima, S. Chaiyakun, Oblique angle deposition of nanocolumnar TiZrN films via reactive magnetron co-sputtering technique: the influence of the Zr target powers, Curr. Appl. Phys. 19 (2019) 894–901, https://doi.org/10.1016/j.cap.2019.05.002.

[42] S. Liedtke-Grüner, C. Grüner, A. Lotnyk, J.W. Gerlach, M. Mensing, P. Schumacher, B. Rauschenbach, Crystallinity and texture of molybdenum thin films obliquely deposited at room temperature, Thin Solid Films 685 (2019) 8–16, https://doi.org/10.1016/j.tsf.2019.05.062.

[43] S. Liedtke, C. Grüner, A. Lotnyk, B. Rauschenbach, Glancing angle deposition of sculptured thin metal films at room temperature, Nanotechnology. 28 (2017) 385604, https://doi.org/10.1088/1361-6528/aa7a79.

[44] S. Liedtke, C. Grüner, J.W. Gerlach, A. Lotnyk, B. Rauschenbach, Crystalline Ti-nanostructures prepared by oblique angle deposition at room temperature, J. Vac. Sci. Technol. B, Nanotechnol. Microelectron. Mater. Process. Meas. Phenom. 36 (2018) 031804, https://doi.org/10.1116/1.5025013.

[45] Z. Qi, J. Tang, J. Huang, D. Zemlyanov, V.G. Pol, H. Wang, Li_2MnO_3 thin films with tilted domain structure as cathode for Li-ion batteries, ACS Appl. Energy Mater. 2 (2019) 3461–3468, https://doi.org/10.1021/acsaem.9b00259.

[46] M. Auer, D. Ye, Facet-mediated growth of silver nanoparticles on biaxial calcium fluoride nanorod arrays, Nanotechnology. 28 (2017), 035301, https://doi.org/10.1088/1361-6528/28/3/035301.

[47] C. Amaya, J.J. Prías-Barragán, W. Aperador, M.A. Hernández-Landaverde, M. Ramírez-Cardona, J.C. Caicedo, L.A. Rodríguez, E. Snoeck, M.E. Gómez, G. Zambrano, Thermal conductivity of yttria-stabilized zirconia thin films with a zigzag microstructure, J. Appl. Phys. 121 (2017) 245110, https://doi.org/10.1063/1.4990283.

[48] P. Nuchuay, T. Chaikeeree, M. Horprathum, N. Mungkung, N. Kasayapanand, C. Oros, S. Limwichean, N. Nuntawong, C. Chananonnawathorn, V. Patthanasettakul, P. Muthitamongkol, B. Samransuksamer, S. Denchitcharoen, A. Klamchuen, C. Thanachayanont, P. Eiamchai, Engineered omnidirectional antireflection ITO nanorod films with super hydrophobic surface via glancing-angle ion-assisted electron-beam evaporation deposition, Curr. Appl. Phys. 17 (2017) 222–229, https://doi.org/10.1016/j.cap.2016.11.018.

[49] S. Zhao, Z. Mi, Recent advances on p-type III-nitride nanowires by molecular beam epitaxy, Crystals 7 (2017) 18–26, https://doi.org/10.3390/cryst7090268.

[50] R.K. Debnath, R. Meijers, K. Jeganathan, T. Richter, T. Stoica, R. Calarco, H. Lüth, Self-assembled growth of GaN nanowires, J. Phys. Conf. Ser. 126 (2008), 012026, https://doi.org/10.1088/1742-6596/126/1/012026.

[51] R.R. Reznik, K.P. Kotlyar, I.P. Soshnikov, S.A. Kukushkin, A.V. Osipov, G. E. Cirlin, MBE growth and structural properties of InAs and InGaAs nanowires with different mole fraction of in on Si and strongly mismatched SiC/Si(111) substrates, Semiconductors. 52 (2018) 651–653, https://doi.org/10.1134/S1063782618050251.

[52] S. Zhao, R. Wang, S. Chu, Z. Mi, Molecular beam epitaxy of III-nitride nanowires: emerging applications from deep-ultraviolet light emitters and Micro-LEDs to artificial photosynthesis, IEEE Nanotechnol. Mag. 13 (2019) 6–16, https://doi.org/10.1109/MNANO.2019.2891370.

[53] O.Y. Koval, G.A. Sapunov, V.V. Fedorov, I.S. Mukhin, Growth and optical properties of GaPN/GaP heterostructure nanowire array, J. Phys. Conf. Ser. 1400 (2019), 055036, https://doi.org/10.1088/1742-6596/1400/5/055036.

[54] S. Morkötter, S. Funk, M. Liang, M. Döblinger, S. Hertenberger, J. Treu, D. Rudolph, A. Yadav, J. Becker, M. Bichler, G. Scarpa, P. Lugli, I. Zardo, J. J. Finley, G. Abstreiter, G. Koblmüller, Role of microstructure on optical properties in high-uniformity $In_{1-x}Ga_xAs$ nanowire arrays: evidence of a wider wurtzite band gap, Phys. Rev. B - Condens. Matter Mater. Phys. 87 (2013) 205303, https://doi.org/10.1103/PhysRevB.87.205303.

[55] E.A. Anyebe, M. Kesaria, A.M. Sanchez, Q. Zhuang, A comparative study of graphite and silicon as suitable substrates for the self-catalysed growth of InAs nanowires by MBE, Appl. Phys. A Mater. Sci. Process. 126 (2020) 427, https://doi.org/10.1007/s00339-020-03609-z.

[56] N. Abdel All, M. Almokhtar, J. El Ghoul, Temperature dependence of photoluminescence from AlN/GaN-thin nanowires, J. Mater. Sci. Mater. Electron. 31 (2020) 5033–5039, https://doi.org/10.1007/s10854-020-03102-6.

[57] B.V. Novikov, S.Y. Serov, N.G. Filosofov, I.V. Shtrom, V.G. Talalaev, O. F. Vyvenko, E.V. Ubyivovk, Y.B. Samsonenko, A.D. Bouravleuv, I.P. Soshnikov, N. V. Sibirev, G.E. Cirlin, V.G. Dubrovskii, Photoluminescence properties of GaAs nanowire ensembles with zincblende and wurtzite crystal structure, Phys. Status Solidi - Rapid Res. Lett. 4 (2010) 175–177, https://doi.org/10.1002/pssr.201004185.

[58] L. Weaver, Cross-section TEM sample preparation of multilayer and poorly adhering films, Microsc. Res. Tech. 36 (1997) 368–371, https://doi.org/10.1002/(SICI)1097-0029(19970301)36:5<368::AID-JEMT4>3.0.CO;2-H.

[59] J.P. Mccaffrey, A. Barna, Preparation of cross-sectional TEM samples for low-angle ion milling, Microsc. Res. Tech. 36 (1997) 362–367, https://doi.org/10.1002/(SICI)1097-0029(19970301)36:5<362::AID-JEMT3>3.0.CO;2-N.

[60] S.A. Bradley, J.F. Reddy, W.E. King, Two methods for aligning a mechanical dimpling device for TEM sample preparation, J. Electron Microsc. Tech. 6 (1987) 303–304, https://doi.org/10.1016/S0016-7878(96)80064-2.

[61] R.E. Flutie, TEM/STEM sample preparation for the investigation of solid state structures: applications to electronic devices and computer components, MRS Proc. 62 (1986) 105–112, https://doi.org/10.1557/PROC-62-105.

[62] G. Sáfrán, T. Grenet, Novel method for the plan-view TEM preparation of thin samples on brittle substrates by mechanical and ion beam thinning, Microsc. Res. Tech. 56 (2002) 308–314, https://doi.org/10.1002/jemt.10034.

[63] O. Unal, A.H. Heuer, T.E. Mitchell, Preparation of crosssectional specimens of ceramic thermal barrier coatings for transmission electron microscopy, J. Electron Microsc. Tech. 14 (1990) 307–312, https://doi.org/10.1002/jemt.1060140404.

[64] H.-W. Cha, M.-C. Kang, K. Shin, C.-W. Yang, Transmission electron microscopy specimen preparation of delicate materials using tripod polisher, Appl. Microsc. 46 (2016) 110–115, https://doi.org/10.9729/am.2016.46.2.110.

[65] P.M. Voyles, J.L. Grazul, D.A. Muller, Imaging individual atoms inside crystals with ADF-STEM, Ultramicroscopy. 96 (2003) 251–273, https://doi.org/10.1016/S0304-3991(03)00092-5.

[66] J. Li, T. Malis, S. Dionne, Recent advances in FIB-TEM specimen preparation techniques, Mater. Charact. 57 (2006) 64–70, https://doi.org/10.1016/j.matchar.2005.12.007.

[67] T.M.C. Dinh, A. Barnabé, M.A. Bui, C. Josse, T. Hungria, C. Bonningue, L. Presmanes, P. Tailhades, FIB plan view lift-out sample preparation for TEM characterization of periodic nanostructures obtained by spinodal decomposition in $Co_{1.7}Fe_{1.3}O_4$ thin films, CrystEngComm. 20 (2018) 6146–6155, https://doi.org/10.1039/c8ce01186a.

[68] Y. Xu, L. Gu, Y. Li, B. Mo, Y. Lin, Combination of focused ion beam (FIB) and microtome by ultrathin slice preparation for transmission electron microscopy (TEM) observation, Earth Planets Sp. 70 (2018) 150, https://doi.org/10.1186/s40623-018-0920-7.

[69] Y. Pan, Y. Zhao, P.K. Tan, Z. Mai, F. Rival, J. Lam, Problems of and solutions for coating techniques for tem sample preparation on ultra low-k dielectric devices after progressive-FIB cross-section analysis, in: Proc. Int. Symp. Phys. Fail. Anal. Integr. Circuits, IPFA, 2018, https://doi.org/10.1109/IPFA.2018.8452598, 2018-July.

[70] T. Malis, S.C. Cheng, R.F. Egerton, EELS log-ratio technique for specimen-thickness measurement in the TEM, J. Electron Microsc. Tech. 8 (1988) 193–200, https://doi.org/10.1002/jemt.1060080206.

[71] S. Rubanov, P.R. Munroe, FIB-induced damage in silicon, J. Microsc. 214 (2004) 213–221, https://doi.org/10.1111/j.0022-2720.2004.01327.x.

[72] Z. Tong, X. Jiang, X. Luo, Q. Bai, Z. Xu, L. Blunt, Y. Liang, Review on FIB-induced damage in diamond materials, Curr. Nanosci. 12 (2016) 685–695, https://doi.org/10.2174/1573413712666160530105707.

[73] P. Nowakowski, C.S. Bonifacio, M.J. Campin, M.L. Ray, P.E. Fischione, Accurate removal of implanted gallium and amorphous damage from TEM specimens after focused ion beam (FIB) preparation, Microsc. Microanal. 23 (2017) 300–301, https://doi.org/10.1017/s1431927617002185.

[74] J. Liu, R. Niu, J. Gu, M. Cabral, M. Song, X. Liao, Effect of ion irradiation introduced by focused ion-beam milling on the mechanical behaviour of sub-micron-sized samples, Sci. Rep. 10 (2020) 10324, https://doi.org/10.1038/s41598-020-66564-y.

[75] X. Zhong, C.A. Wade, P.J. Withers, X. Zhou, C. Cai, S.J. Haigh, M.G. Burke, Comparing Xe^+pFIB and Ga^+FIB for TEM sample preparation of Al alloys: Minimising FIB-induced artefacts, J. Microsc. 282 (2021) 101–112, https://doi.org/10.1111/jmi.12983.

[76] P. Roediger, H.D. Wanzenboeck, S. Waid, G. Hochleitner, E. Bertagnolli, Focused-ion-beam-inflicted surface amorphization and gallium implantation-new insights and removal by focused-electron-beam-induced etching, Nanotechnology. 22 (2011) 235302, https://doi.org/10.1088/0957-4484/22/23/235302.

[77] J. Dervaux, P.A. Cormier, P. Moskovkin, O. Douheret, S. Konstantinidis, R. Lazzaroni, S. Lucas, R. Snyders, Synthesis of nanostructured Ti thin films by combining glancing angle deposition and magnetron sputtering: a joint

experimental and modeling study, Thin Solid Films 636 (2017) 644–657, https://doi.org/10.1016/j.tsf.2017.06.006.
[78] V. Collado, N. Martin, P. Pedrosa, J.Y. Rauch, M. Horakova, M.A.P. Yazdi, A. Billard, Temperature dependence of electrical resistivity in oxidized vanadium films grown by the GLAD technique, Surf. Coatings Technol. 304 (2016) 476–485, https://doi.org/10.1016/j.surfcoat.2016.07.057.
[79] G. Abadias, F. Anğay, R. Mareus, C. Mastail, Texture and stress evolution in HfN films sputter-deposited at oblique angles, Coatings. 9 (2019) 712, https://doi.org/10.3390/coatings9110712.
[80] P. Shi, X. Li, Q. Zhang, Z. Yi, J. Luo, Photocatalytic activity of self-assembled porous TiO_2 nano-columns array fabricated by oblique angle sputter deposition, Mater. Res. Express. 5 (2018), 045018, https://doi.org/10.1088/2053-1591/aaba57.
[81] K. Upadhyaya, N. Ayachit, S.M. Shivaprasad, Comparison of optoelectronic properties of epitaxial and non-epitaxial GaN nanostructures, J. Mater. Sci. Mater. Electron. 31 (2020) 13756–13764, https://doi.org/10.1007/s10854-020-03935-1.
[82] J.L. Rouviere, J.L. Weyher, M. Seelmann-Eggebert, S. Porowski, Polarity determination for GaN films grown on (0001) sapphire and high-pressure-grown GaN single crystals, Appl. Phys. Lett. 73 (1998) 668–670, https://doi.org/10.1063/1.121942.
[83] M. Losurdo, M.M. Giangregorio, P. Capezzuto, G. Bruno, G. Namkoong, W. A. Doolittle, A.S. Brown, Interplay between GaN polarity and surface reactivity towards atomic hydrogen, J. Appl. Phys. 95 (2004) 8408–8418, https://doi.org/10.1063/1.1745124.
[84] J.L. Weyher, S. Müller, I. Grzegory, S. Porowski, Chemical polishing of bulk and epitaxial GaN, J. Cryst. Growth 182 (1997) 17–22, https://doi.org/10.1016/S0022-0248(97)00320-5.
[85] R. Dimitrov, M. Murphy, J. Smart, W. Schaff, J.R. Shealy, L.F. Eastman, O. Ambacher, M. Stutzmann, Two-dimensional electron gases in Ga-face and N-face AlGaN/GaN heterostructures grown by plasma-induced molecular beam epitaxy and metalorganic chemical vapor deposition on sapphire, J. Appl. Phys. 87 (2000) 3375–3380, https://doi.org/10.1063/1.372353.
[86] S. Rajan, M. Wong, Y. Fu, F. Wu, J.S. Speck, U.K. Mishra, Growth and electrical characterization of N-face AlGaN/GaN heterostructures, Japanese J. Appl. Physics, Part 2 Lett. 44 (2005) 15–18, https://doi.org/10.1143/JJAP.44.L1478.
[87] F. Tuomisto, K. Saarinen, B. Lucznik, I. Grzegory, H. Teisseyre, T. Suski, S. Porowski, P.R. Hageman, J. Likonen, Effect of growth polarity on vacancy defect and impurity incorporation in dislocation-free GaN, Appl. Phys. Lett. 86 (2005), 031915, https://doi.org/10.1063/1.1854745.
[88] H.M. Ng, A.Y. Cho, Investigation of Si doping and impurity incorporation dependence on the polarity of GaN by molecular beam epitaxy, J. Vac. Sci. Technol. B Microelectron. Nanom. Struct. 20 (2002) 1217, https://doi.org/10.1116/1.1463723.
[89] D. Muto, T. Araki, H. Naoi, F. Matsuda, Y. Nanishi, Polarity determination of InN by wet etching, Phys. Status Solidi Appl. Mater. Sci. 202 (2005) 773–776, https://doi.org/10.1002/pssa.200461439.
[90] O. Romanyuk, I. Bartoš, J. Brault, P. De Mierry, T. Paskova, P. Jiříček, GaN quantum dot polarity determination by X-ray photoelectron diffraction, Appl. Surf. Sci. 389 (2016) 1156–1160, https://doi.org/10.1016/j.apsusc.2016.07.169.
[91] M. De La Mata, C. Magen, J. Gazquez, M.I.B. Utama, M. Heiss, S. Lopatin, F. Furtmayr, C.J. Fernández-Rojas, B. Peng, J.R. Morante, R. Rurali, M. Eickhoff, A. Fontcuberta, I. Morral, Q. Xiong, J., Arbiol, polarity assignment in ZnTe, GaAs, ZnO, and GaN-AlN nanowires from direct dumbbell analysis, Nano Lett. 12 (2012) 2579–2586, https://doi.org/10.1021/nl300840q.
[92] F. Schuster, B. Laumer, R.R. Zamani, C. Magén, J.R. Morante, J. Arbiol, M. Stutzmann, P-GaN/n-ZnO heterojunction nanowires: optoelectronic properties and the role of interface polarity, ACS Nano 8 (2014) 4376–4384, https://doi.org/10.1021/nn406134e.
[93] S.Y. Woo, M. Bugnet, H.P.T. Nguyen, Z. Mi, G.A. Botton, Atomic ordering in InGaN alloys within nanowire heterostructures, Nano Lett. 15 (2015) 6413–6418, https://doi.org/10.1021/acs.nanolett.5b01628.
[94] A.T.M.G. Sarwar, F. Yang, B.D. Esser, T.F. Kent, D.W. McComb, R.C. Myers, Self-assembled InN micro-mushrooms by upside-down pendeoepitaxy, J. Cryst. Growth 443 (2016) 90–97, https://doi.org/10.1016/j.jcrysgro.2016.03.030.
[95] G. Naresh-Kumar, J. Bruckbauer, A. Winkelmann, X. Yu, B. Hourahine, P. R. Edwards, T. Wang, C. Trager-Cowan, R.W. Martin, Determining GaN nanowire polarity and its influence on light emission in the scanning electron microscope, Nano Lett. 19 (2019) 3863–3870, https://doi.org/10.1021/acs.nanolett.9b01054.
[96] P. Rajak, M. Islam, J.J. Jiménez, J.M. Mánuel, P. Aseev, E. Calleja Gačević, R. García, F.M. Morales, S. Bhattacharyya, Unravelling the polarity of InN quantum dots using a modified approach of negative-spherical-aberration imaging, Nanoscale 11 (2019) 13632–13638, https://doi.org/10.1039/c9nr04146j.
[97] B. Zhao, M.N. Lockrey, P. Caroff, N. Wang, L. Li, J. Wong-Leung, H.H. Tan, C. Jagadish, The effect of nitridation on the polarity and optical properties of GaN self-assembled nanorods, Nanoscale. 10 (2018) 11205–11210, https://doi.org/10.1039/c8nr00737c.
[98] I. Lazić, E.G.T. Bosch, Analytical review of direct STEM imaging techniques for thin samples, 1st ed., Elsevier Inc., 2017.
[99] I. Lazić, E.G.T. Bosch, S. Lazar, Phase contrast STEM for thin samples: integrated differential phase contrast, Ultramicroscopy. 160 (2016) 265–280, https://doi.org/10.1016/j.ultramic.2015.10.011.
[100] E. Yücelen, I. Lazić, E.G.T. Bosch, Phase contrast scanning transmission electron microscopy imaging of light and heavy atoms at the limit of contrast and resolution, Sci. Rep. 8 (2018) 2676, https://doi.org/10.1038/s41598-018-20377-2.
[101] R.F. Egerton, M. Malac, EELS in the TEM, J. Electron Spectros. Relat. Phenomena. 143 (2005) 43–50, https://doi.org/10.1016/j.elspec.2003.12.009.
[102] G. Bertoni, J. Verbeeck, Accuracy and precision in model based EELS quantification, Ultramicroscopy. 108 (2008) 782–790, https://doi.org/10.1016/j.ultramic.2008.01.004.
[103] R. Leapman, EELS quantitative analysis, in: C.C. Ahn (Ed.), Transmission Electron Energy Loss Spectrometry in Materials Science and The EELS Atlas, Second edition, Wiley, 2004, pp. 49–96.
[104] M. Weyland, P.A. Midgley, Electron tomography, Mater. Today 7 (2004) 32–40, https://doi.org/10.1016/S1369-7021(04)00569-3.
[105] P.A. Midgley, R.E. Dunin-Borkowski, Electron tomography and holography in materials science, Nat. Mater. 8 (2009) 271–280, https://doi.org/10.1038/nmat2406.
[106] B. Goris, T. Roelandts, K.J. Batenburg, H. Heidari Mezerji, S. Bals, Advanced reconstruction algorithms for electron tomography: from comparison to combination, Ultramicroscopy. 127 (2013) 40–47, https://doi.org/10.1016/j.ultramic.2012.07.003.
[107] W. van Aarle, W.J. Palenstijn, J. De Beenhouwer, T. Altantzis, S. Bals, K. J. Batenburg, J. Sijbers, The ASTRA toolbox: a platform for advanced algorithm development in electron tomography, Ultramicroscopy. 157 (2015) 35–47, https://doi.org/10.1016/j.ultramic.2015.05.002.
[108] D. Chen, B. Goris, F. Bleichrodt, H.H. Mezerji, S. Bals, K.J. Batenburg, G. de With, H. Friedrich, The properties of SIRT, TVM, and DART for 3D imaging of tubular domains in nanocomposite thin-films and sections, Ultramicroscopy. 147 (2014) 137–148, https://doi.org/10.1016/j.ultramic.2014.08.005.
[109] C. Kübel, A. Voigt, R. Schoenmakers, M. Otten, D. Su, T.C. Lee, A. Carlsson, J. Bradley, Recent advances in electron tomography: TEM and HAADF-STEM tomography for materials science and semiconductor applications, Microsc. Microanal. 11 (2005) 378–400, https://doi.org/10.1017/S1431927605050361.
[110] P.A. Midgley, M. Weyland, J. Meurig Thomas, B.F.G. Johnson, Z-contrast tomography: a technique in three-dimensional nanostructural analysis based on Rutherford scattering, Chem. Commun. (2001) 907–908, https://doi.org/10.1039/b101819c.
[111] H. Friedrich, M.R. McCartney, P.R. Buseck, Comparison of intensity distributions in tomograms from BF TEM, ADF STEM, HAADF STEM, and calculated tilt series, Ultramicroscopy. 106 (2005) 18–27, https://doi.org/10.1016/j.ultramic.2005.06.005.
[112] J. Hernández-Saz, M. Herrera, S.I. Molina, Fabrication of needle-shaped specimens containing subsurface nanostructures for electron tomography, in: Z. M. Wang (Ed.), FIB Nanostructures vol. 20, Springer, 2013, pp. 241–246.